Chapter 4

Dynamics

It is the beauty of two-photon photoemission that we can not only observe the empty states of the electronic band structure, but with a variation of the delay between pump and probe pulse also access their dynamic behaviour. Figure 4.1 shows spectra of spin- and energy-resolved 2PPE measurements taken at increasing pump-probe delay. In all image-potential-state peaks the intensity decreases exponentially with time, fastest in the $n = 1$ state. The $n = 2$ peak decays on a slower time scale and after about 120 fs the intensity of the third image-potential state exceeds the remaining intensity of the second state because the population in the $n = 3$ state lives even longer. What can also be noted is the faster decay of the minority components compared with that of the majority components. This is most obvious for the second image-potential state where the intensity of the majority component overtakes the minority intensity after approximately 120 fs.

In the following sections we will discuss the spin-dependent dynamics of electrons in the image-potential states in detail, but first we will introduce the theoretical model used for the description of the 2PPE process.

4.1   Optical Bloch Equations

The lifetimes of states observed with 2PPE may be of the order of or even shorter than the duration of the laser pulses used in the experiment. Decay of the population and transitions between excited states occur during the excitation into the final state above the vacuum energy, while the pump pulse may still be active. We can therefore in general not treat 2PPE as a process
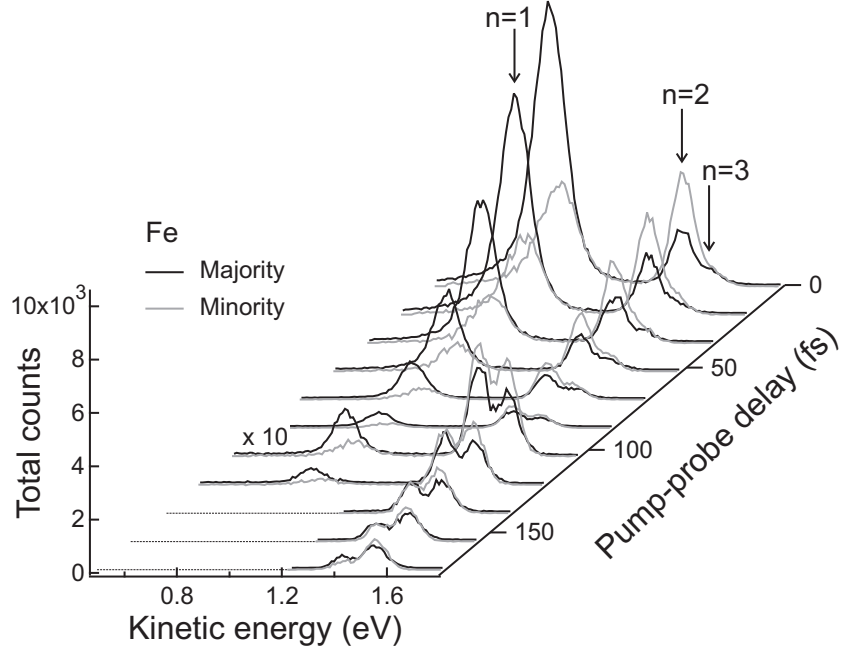
Figure 4.1: Spectra of energy-resolved measurements at increasing pump-probe delay. The majority component is displayed in black, the minority component in grey.

of two consecutive and independent photo-excitation steps[1]. However, the density matrix formalism is perfectly capable of dealing with these effects [21, 103, 28].

The energy diagram for a 2PPE process is shown schematically in Fig. 4.2. The pump pulse with energy $\hbar\omega_a$ excites electrons from the initial state $|i\rangle$ into an intermediate state $|1\rangle, |2\rangle, \ldots, |N\rangle$, and after a time T_d the probe pulse $\hbar\omega_b$ raises the electrons above the vacuum energy E_{vac} into the final state $|f\rangle$.

In the unperturbed case, the electronic states have a random phase relation. The interaction with the laser fields induces a coherence between the participating states, i.e. a superposition of the electronic states $|n\rangle$, $n \in \{i, 1, 2, \ldots, N, f\}$ with a fixed phase $a_n(t)$

$$|\Psi\rangle = \sum_n a_n(t)|n\rangle. \tag{4.1}$$

If the state $|n\rangle$ has a lifetime $\tau_n = 1/\Gamma_n$ the population in the state must

---

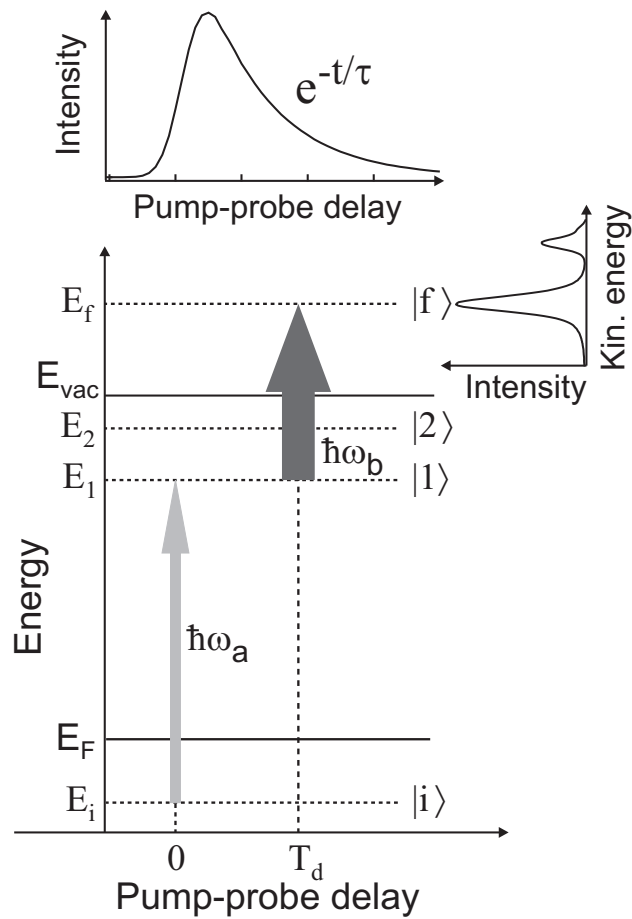[1]In the case of bichromatic 2PPE, we may at least neglect coherence effects between the two laser pulses

Figure 4.2: Schematic of the 2PPE for the simulation; indicated are the pump and probe pulse with energies $\hbar\omega_a$ and $\hbar\omega_b$, one initial state $|i\rangle$, one final state $|f\rangle$, and two intermediate states $|1\rangle$ and $|2\rangle$. The upper spectrum is simulated at a fixed final state energy E_f with varying delay T_d. For the spectrum on the right E_f was varied at constant T_d, integrating over a continuum of initial states.

decay as[2]

$$|a_n(t)|^2 = |a_n(0)|^2 e^{-\Gamma_n t}. \tag{4.2}$$

Hence $a_n(t)$ develops in the absence of the laser fields as

$$a_n(t) = a_n(0)e^{-\Gamma_n t/2}e^{-iE_n t/\hbar}e^{i\phi_n(t)}. \tag{4.3}$$

The quantity $\phi_n(t)$ describes additional phase-breaking events (such as elastic defect scattering) that are not accompanied by a change in the population [28, 161]. ϕ_n is associated with what will be later introduced as the (pure) dephasing rate Γ_{mn}^*. Even after the pump process, the probe pulse samples the time-dependent population $|a_n(t)|^2$ of the intermediate states, in fundamental contrast to regular photoemission, where the population of the initial occupied state is constant [55]. The two-photon photoemission intensity recorded in our experiment basically resembles the population of the final state $|a_f(t)|^2$.

Formally, the 2PPE process may be modelled with the Liouville – von Neumann equations in the framework of the density matrix formalism [21, 103, 28, 180, 22]. The elements of the density matrix $\rho_{mn} = \langle a_m a_n \rangle$ (ρ_{mn} is constructed from the basis $\{|n\rangle\}$ and $\langle\rangle$ denotes the ensemble average) can be interpreted as follows: The diagonal elements ρ_{nn} give the probability that the system is found in the energy eigenstate $|n\rangle$, or in an ensemble the average population of this state. The coherence between states $|m\rangle$ and $|n\rangle$ is given by the off-diagonal elements ρ_{mn}. When a laser field induces a coherent superposition between states, the off-diagonal elements are proportional to the polarisation, i.e. the induced dipole moment in the system.

The density matrix equation of motion with the phenomenological inclusion of dissipation is given by

$$\dot{\rho}_{mn} = -\frac{i}{\hbar}[H_0 + H_{\text{int}}, \rho]_{mn} - \gamma_{mn}\rho_{mn}; \quad m \neq n$$

$$\dot{\rho}_{nn} = -\frac{i}{\hbar}[H_0 + H_{\text{int}}, \rho]_{nn} + \sum_m \Gamma_{nm}\rho_{mm} - \Gamma_n\rho_{nn} , \tag{4.4}$$

where H_0 is the unperturbed Hamiltonian of the system with $H_0|n\rangle = E_n|n\rangle$. H_{int} describes the interaction with the laser field as introduced in Section 3.4, but now with the electric field consisting of pump and probe pulse $\mathbf{A}(t) = \mathbf{A}_a(t - T_d) + \mathbf{A}_b(t)$. As already mentioned at the beginning of this section, the population ρ_{nn} decays with the rate $\Gamma_n = 1/\tau_n$. Refilling of state $|n\rangle$

_____

[2]It has been shown in e.g. Reference [160] that the decay of a single image-potential state proceeds indeed exponentially.

from other levels $|m\rangle$ occurs with Γ_{nm}. The damping rate of the off-diagonal elements

$$\gamma_{mn} = \frac{1}{2}(\Gamma_m + \Gamma_n) + \Gamma^*_{mn} \tag{4.5}$$

accounts for the relaxation of the ρ_{mn} coherence. Note that the population decay also causes decoherence, but the so-called *pure* dephasing rate Γ^*_{mn} leaves the population unchanged.

Henceforth $n, m, k \in \{1, 2, \ldots, N\}$ will refer to intermediate states only, while i and f denote an initial and a final state, respectively. We retain only terms with small detuning:

$$\begin{aligned}
\Delta^a_n &= \hbar\omega_a - (E_n - E_i) \\
\Delta^b_n &= \hbar\omega_b - (E_f - E_n) \\
\Delta^{ab} &= \hbar\omega_a + \hbar\omega_b - (E_f - E_i) \, ,
\end{aligned} \tag{4.6}$$

i.e. terms with photon energies close to the resonance energy between two levels. Hence the pump pulse $\mathbf{A}_a(t - T_d)$ mediates dipole transitions only between initial state $|i\rangle$ and intermediate states $|n\rangle$ and the probe pulse $\mathbf{A}_b(t)$ between $|n\rangle$ and final state $|f\rangle$. Also a direct transition between initial and final state can occur through simultaneous absorption of a pump and a probe photon. The corresponding optical matrix elements M_{ni}, M_{fn}, M_{fi} have already been defined in Equation 3.4.

By introducing the slowly varying quantities

$$\begin{aligned}
\tilde{\rho}_{in} &\equiv e^{-i\omega_a t}\rho_{in} \\
\tilde{\rho}_{nf} &\equiv e^{-i\omega_b t}\rho_{nf} \\
\tilde{\rho}_{if} &\equiv e^{-i(\omega_a + \omega_b)t}\rho_{if} \, ,
\end{aligned} \tag{4.7}$$

and neglecting all fast oscillating terms in the rotating wave approximation [28], the system of differential Equations 4.4 can be simplified to what

is commonly known as optical Bloch equations:

$$\dot{\rho}_{ii} = +\frac{1}{\hbar}\sum_n \text{Im}(M_{ni}\tilde{\rho}_{in})$$

$$\dot{\rho}_{mn} = \frac{i}{2\hbar}(M_{mi}\tilde{\rho}_{in} - M_{in}\tilde{\rho}_{im}^*) - \frac{i}{2\hbar}(M_{fn}\tilde{\rho}_{mf} - M_{mf}\tilde{\rho}_{nf}^*) - \rho_{mn}\gamma_{mn}$$
$$(\text{for } m \neq n)$$

$$\dot{\rho}_{nn} = -\frac{1}{\hbar}\text{Im}(M_{ni}\tilde{\rho}_{in}) + \frac{1}{\hbar}\text{Im}(M_{fn}\tilde{\rho}_{nf}) - \rho_{nn}\Gamma_{nn} + \sum_k \Gamma_{nk}\rho_{kk}$$

$$\dot{\rho}_{ff} = -\frac{1}{\hbar}\sum_n \text{Im}(M_{fn}\tilde{\rho}_{nf})$$

$$\dot{\tilde{\rho}}_{in} = -\frac{i}{\hbar}\Delta_n^a \tilde{\rho}_{in} - \frac{i}{2\hbar}M_{fn}\tilde{\rho}_{if} - \frac{i}{2\hbar}(M_{in}\rho_{ii} - \sum_k M_{ik}\rho_{kn}) - \tilde{\rho}_{in}(\frac{1}{2}\Gamma_n + \Gamma_{in}^*)$$

$$\dot{\tilde{\rho}}_{nf} = -\frac{i}{\hbar}\Delta_n^b \tilde{\rho}_{nf} + \frac{i}{2\hbar}M_{ni}\tilde{\rho}_{if} - \frac{i}{2\hbar}(\sum_k M_{kf}\rho_{nk} - M_{nf}\rho_{ff})$$

$$\qquad -\tilde{\rho}_{nf}(\frac{1}{2}\Gamma_n + \Gamma_{nf}^*)$$

$$\dot{\tilde{\rho}}_{if} = -\frac{i}{\hbar}\Delta^{ab}\tilde{\rho}_{if} + \frac{i}{2\hbar}\sum_k (M_{ik}\tilde{\rho}_{kf} - M_{kf}\tilde{\rho}_{ik}) - \tilde{\rho}_{if}\Gamma_{if}^* \ . \qquad (4.8)$$

Only in a few special cases can these equations be solved analytically for a three level system [183, 24].

We will not discuss the sometimes quite surprising features of the solutions of Equations 4.8 here any further, but rather where necessary for the interpretation of the experimental data.

Usually the optical Bloch equations are solved numerically, and the solution by Boger [22] will be employed for the simulations in the following sections. Of the parameters entering the simulations, as many as possible were collected from independent experiments. The pulse length of the probe pulse was determined by interferometric autocorrelation measurements (cf. Section 2.1.1). Further, a Gaussian shaped envelope of the pump and probe pulse is assumed. This choice is strongly supported by measurements of the linewidth versus pump-probe delay of the $n = 1$ image-potential state on Cu(100) (not shown) [24]. The cross-correlation trace obtained by two-photon photoemission from the occupied surface state on Cu(111) directly follows the time profile of the pump and probe pulse, providing a measure of the pump pulse length (for known probe pulse length), and also a precise measurement of the time zero $T_d = 0$ between pump and probe pulse. Two-photon absorption of the occupied $n = 0$ state on Cu(111) is affected by off-resonant excitation of the intermediate $n = 1$ image-potential state
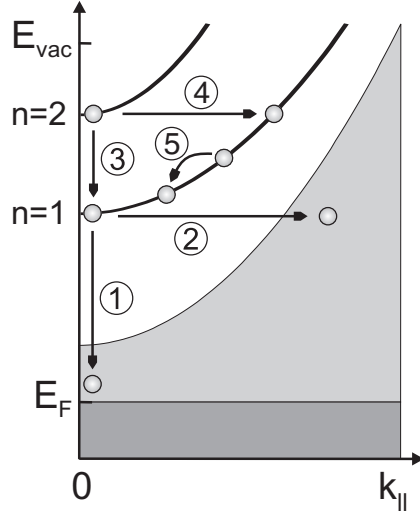
Figure 4.3: Schematic of the free-electron like dispersion parallel to the surface of the $n = 1$ and $n = 2$ image-potential state in the gap of the surface-projected bulk bands (gray area). Possible processes involved in the population decay are indicated.

and depends on the detuning Δ_n^a and thus on the pump pulse photon energy $\hbar\omega_a$ (cf. Equation 4.6). The finite lifetime of the $n = 1$ image-potential state leads to a shift of the cross-correlation trace and apparent time zero but can be accounted for in the simulation. Thus, with the help of the simulation, lifetimes considerably shorter than the laser pulse duration can be analysed [74].

Unless stated otherwise, the excitation in the simulation takes place from a continuum of equally distributed initial states. This of course disregards effects of the initial-state band structure, which will be discussed in more detail in Section 4.4.1.

Figure 4.3 schematically depicts the free-electron like dispersion of the image-potential states parallel to the surface, as well as the surface-projected bulk bands, filled states in dark, empty states in light grey. The most common decay processes comprise inelastic decay into bulk states (1), elastic decay into bulk states (2), inelastic interband scattering (3) and elastic interband scattering (4) from higher to lower lying image-potential states and inelastic intraband decay within one image-potential band (5). We speak of elastic, or rather quasi-elastic processes, if the energy transfer during the scattering process is smaller than our experimental resolution so that the electron remains within the detection window set by the finite angle and energy resolution. Scattering processes with higher energy transfer (and arbitrary momentum

transfer) are hence termed inelastic.

4.2   Spin-dependent lifetimes

For a single electron excited in a solid several interaction processes exist,
which determine its transient behaviour and contribute to its finite lifetime.
While in a semiconductor scattering with phonons and defects provide the
major channels for relaxation of energy and momentum [8], in a metal, due
to its high density of electrons at the Fermi level, decay occurs mainly via
screened Coulomb interaction with the other electrons in the system [51].
Self-consistent calculations of the interaction of an excited electron with a
free electron gas yield the well-known Fermi-liquid behaviour for the inelastic
lifetime of hot electrons at an energy E above the Fermi energy [140, 144]

$$\tau(E) \propto n_0^{5/6}(E - E_F)^{-2} \ . \tag{4.9}$$

The hot-electron lifetime τ is determined by a competition between tran-
sitions and screening. While the increasing number of states available for
scattering is mirrored by the quadratic energy dependence, a high valence-
electron density n_0 leads to strong screening and consequently to an increase
in the lifetime.

Image-potential-state energies lie roughly 4 eV above the Fermi level and
from theoretical studies based on Fermi-liquid theory (e.g. [32]), lifetimes of
below 5 fs are expected for hot electrons at these energies. However, the
time-resolved measurements of the $n = 1$ image-potential state shown in
Figure 4.4 reveal lifetimes of $\tau_1^{\uparrow} = 16 \pm 2$ fs and $\tau_1^{\downarrow} = 11 \pm 2$ fs on iron
for the majority- and minority-spin component, respectively. Even longer
lifetimes ($\tau_1^{\uparrow} = 19 \pm 2$ fs and $\tau_1^{\downarrow} = 16 \pm 2$ fs) were found on cobalt. Note
that in these spectra the intensity is plotted on a logarithmic scale, so that
the exponential decay of the population becomes evident in the form of a
straight line at positive pump-probe delay.

In Figure 4.4, the insets schematically depict the free-electron like dispersion
parallel to the surface of the first and second image-potential state. The
shaded area represents the surface-projected bulk band structure. The mea-
surement was carried out at $k_{\parallel} = 0$ and $E_{\mathrm{kin}} = E_1 + \hbar\omega_b - E_{\mathrm{vac}}$, probing the
intermediate state at the point indicated by the dashed circle. Decay of the
population occurs inelastically and (quasi)elastically (vertical and horizontal
arrow) into the bulk states.

The time-resolved experiments were conducted with a pump-photon energy
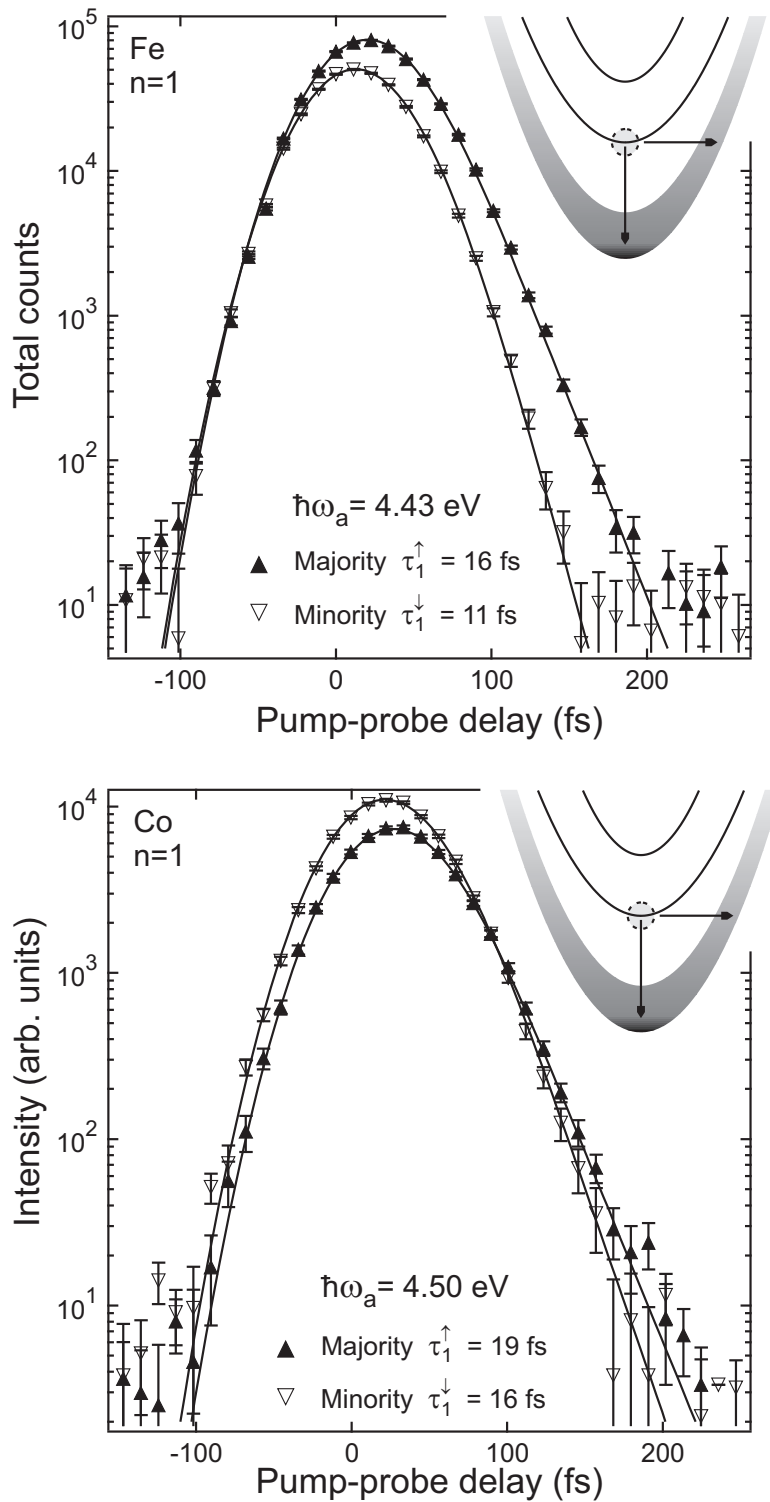only just large enough to populate the $n = 1$ image-potential state at the

Figure 4.4: Time-resolved 2PPE spectrum of the $n = 1$ image-potential state on Fe (top) and Co (bottom) for majority (▲) and minority (▽) electrons. The simulations (solid lines) were done using optical Bloch equations.

minimum of the dispersing band. Thus interband scattering from the $n \geq 2$
into the $n = 1$ image-potential state and intraband scattering from states at
$k_\parallel \neq 0$ to the $\bar{\Gamma}$ point is effectively avoided and the decay of the population
is not perturbed by refilling effects.

The penetration of an image-potential state into the bulk gives a measure
of the coupling of this state to bulk electronic states [36]. In fact, the decay
rate of an image-potential state through electron-hole pair creation may be
approximated by the decay rate of a bulk electron at the same energy times
the fraction of the probability density inside the bulk crystal [49]. As a
major part of the image-potential state resides outside the metal, the weak
interaction with the bulk leads to considerably longer lifetimes, just like we
observed in our experiment.

This may also be one of the reasons why we observe longer lifetimes on Co.
As already mentioned in Section 3.3, the energetic position of the first image-
potential state on Co lies further from the edges of the surface-projected band
gap than on Fe. Hence, on Co we expect a weaker interaction of the $n = 1$
image-potential state with the bulk states, not only leading to the smaller
exchange splitting we have observed, but also to longer lifetimes than on Fe.
In addition the iron films are not annealed and might therefore exhibit de-
fect scattering, which can also cause substantial population decay via elastic
scattering into the bulk states [22].

From Fermi-liquid theory one expects the lifetimes to decrease with increasing
energy, i.e. in our case with increasing quantum number. We already know
from Figure 4.1, however, that the opposite is the case. The lifetime increases
drastically for the image-potential states with higher quantum number. Of
course the penetration of the image-potential states into the bulk and thus
the interaction strength decreases with n^{-3} and this effect by far outweighs
the $(E - E_F)^2$ dependence of the decay rate.

Figure 4.5 shows time-resolved measurements of the second image-potential
state on iron with lifetimes of $\tau_2^\uparrow = 54 \pm 3$ fs and $\tau_2^\downarrow = 43 \pm 3$ fs for majority
and minority electrons, and on cobalt with lifetimes of $\tau_2^\uparrow = 71 \pm 5$ fs and
$\tau_2^\downarrow = 58 \pm 5$ fs, respectively. In each spin channel the lifetimes approximately
obey $\tau_n \propto n^2$. This n^2 dependence is also observed between the $n = 1$
and $n = 2$ image-potential state on the Cu(100) surface [180]. For higher
quantum number n, the lifetime of the image-potential states is governed
by the n^{-3} dependence of the penetration depth, i.e. $\tau_n \propto n^3$, because the
energetic position remains almost constant for $n \geq 3$.

In these measurements, the photon energy must be high enough for an ex-
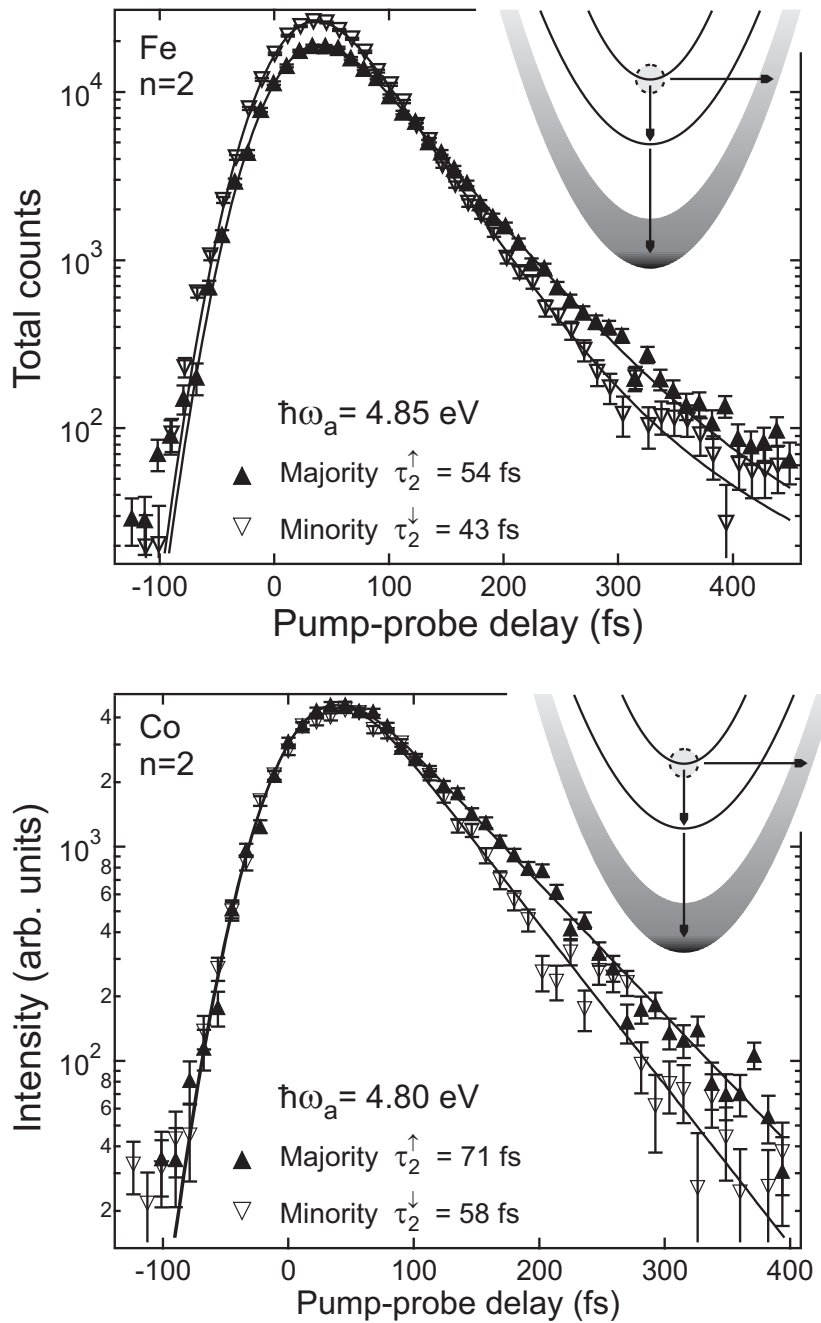citation of the $n = 2$ image-potential state from states below E_F. As the

Figure 4.5: Time-resolved 2PPE spectrum of the $n = 2$ image-potential state on Fe (top) and Co (bottom) for majority (▲) and minority (▽) electrons. The simulations (solid lines) were done using optical Bloch equations.

$n = 3$ image-potential state lies only around 100 meV higher in energy, the large laser bandwidth and intrinsic linewidth of the image-potential states sometimes render it difficult to avoid the simultaneous excitation of higher image-potential states. In the upper panel of Figure 4.5 (Fe) the decay obviously deviates from a simple exponential decay. Here also the $n = 3$ image-potential state is excited and the traces show a biexponential decay due to interband scattering from the $n = 3$ into the $n = 2$ image-potential state. This interband scattering dominates the $n = 2$ population at large pump-probe delay since the lifetime τ_3 exceeds τ_2. Therefore the apparent decay rate of the $n = 2$ state at large pump-probe delay is determined by refilling from the $n = 3$ image-potential state, which in turn depends on the transient population ρ_{33} of the $n = 3$ image-potential state. Hence for $t \gg \tau_2$

$$\rho_{22}(t) \propto \rho_{33}(t) \propto e^{-t/\tau_3} \ . \tag{4.10}$$

Consequently the biexponential decay is described by a time-dependent combination of the decay rates Γ_2 and Γ_3. In fact, lower lying image-potential states contribute considerably to the inelastic decay of the image-potential states with higher quantum number [51]. This can be understood on the basis of the large spatial overlap between the members of the Rydberg-like series as compared to the overlap of the image-potential with bulk states.

Up to now we have not addressed the spin dependence of the lifetimes. As early as 1936, Mott explained the large resistivity of the transition metals Fe, Co and Ni in comparison to Cu with decay of the current carrying delocalised s electrons into empty d states above the Fermi level [113]. The more d states are available, the stronger is this scattering process. If only spin-conserving transitions are allowed, the large number of empty d states in the minority-spin channel leads to preferential scattering of minority electrons. With these assumptions it is easily explained why Fe has the largest resistivity of the three d ferromagnets [167]. As the only "weak" ferromagnet of the three, Fe also has empty *majority* d states above E_F, final states for majority electrons to scatter into. Mott's idea is the basis for the "two current model" (e.g. employed in the theory of magnetoresistance), where transport phenomena in ferromagnets are treated separately in the two spin channels [59].

Of course the existence of empty d states above the Fermi level is not only responsible for the low conductivity of the transition metals but also mainly accounts for the shorter image-potential-state lifetimes observed on Fe and Co compared to Cu with $\tau_1^{\mathrm{Cu}} = 40$ fs [75].

Several theoretical studies underlined the importance of the d states (e.g.

[128, 93, 196]). In first order minority-spin electrons in a ferromagnet decay on a faster time scale than majority electrons due to the different number of majority and minority empty states above E_F. This has already been demonstrated in time- and spin-resolved 2PPE experiments for bulk electrons [2] and via a determination of the spin-dependent linewidth for image-potential electrons on iron [124].

With $\tau^\uparrow/\tau^\downarrow \approx 1.2 - 1.45$ the ratio of spin-up versus spin-down lifetimes in our experiment lies in the same region as those of Refs. [2, 93], and slightly lower than found with IPE on Fe(110), where the spin-dependent linewidths corresponds to $\tau^\uparrow/\tau^\downarrow = 2$ [124]. The linewidth measured with IPE, however, includes not only population decay, but dephasing as well, and we will see in Section 4.4.2 that dephasing of the image-potential state on the fcc Fe(100) surface is also spin dependent.

On the other hand our results deviate strongly from those obtained in magnetic tunnel transistor experiments [174]. With this technique, the inelastic mean free path (IMFP) of hot electrons at low excitation energies can be studied. The majority-to-minority ratio of IMPF measured in $Ni_{80}Fe_{20}$ is $\lambda^\uparrow/\lambda^\downarrow \approx 4 - 5$. Though theoretical calculations attribute the spin asymmetry of the IMFP in Fe mainly to the spin dependence of the velocity v (with $\lambda = v\tau$), they found that the ratio of the *lifetimes* is still considerably closer to 4 at more than 2 eV above E_F [196].

We would like to mention here that our measurements provide access to single scattering events of electrons in well-defined surface states. We have outlined that these lifetimes are related to the lifetimes of corresponding bulk states. By a proper choice of the photon energy we may also exclude refilling processes, which invariably complicate the interpretation of experimental data obtained with bulk electrons. Nevertheless, the observed spin dependence is significantly weaker than predicted by theory. Using simple density of states arguments we would furthermore expect a much more pronounced spin dependence in the strong ferromagnet cobalt than in the weak ferromagnet iron[3].

As the predominant decay process of electrons in a metal is electron-electron scattering, the number of available scattering partners, i.e. bulk electrons ensuring energy and momentum conservation, are crucial for an understanding of the dynamical behaviour of excited electrons. This topic would lead us deep into the realm of many-body decay mechanisms in metals and will resur-

---

[3]From what we know of the band structure of our thin films, the classification of bulk iron and cobalt into weak and strong ferromagnets seems equally true for the thin films studied here [135].

face in connection with inter- and intraband scattering on iron and cobalt. We will therefore continue this discussion in Section 4.6.

Finally, for the interpretation of image-potential-state lifetimes, the existence of intrinsic surface states must also be taken into account. On the Cu(111) surface, the Shockley surface state contributes strongly, i.e. about 40%, to the decay of the image-potential state due to the large spatial overlap of the wave functions [131]. We know of the existence of a minority surface resonance on the cobalt films (cf. Section 3.5), which lies at roughly the same energy below E_F as the $n = 0$ on Cu(111). Preliminary calculations of the band structure of fcc cobalt found this minority-spin surface resonance at 0.45 eV below E_F [30]. They indicate, however, that the state does not cross the Fermi level, as there is no band gap around E_F in the surface-projected bulk band structure supporting the surface resonance. Accordingly this surface resonance can not participate in the decay of the image-potential states on Co, as only unoccupied states may serve as final states. Quantum well states in the thin magnetic films, on the other hand, may very well act as final states in the decay of image-potential-state electrons. Further contributions to the decay of image-state electrons comprise quasi-elastic decay via defect scattering and electron-phonon scattering.

We know from Ref. [22] that 1% of a ML Cu adatoms on the Cu(100) surface increases the decay rate of the $n = 1$ image-potential state by 16% due to elastic defect scattering into the bulk states. A certain amount of defect induced scattering is expected on the iron films as they are not annealed after evaporation. However, we will show in Section 4.5 that defect scattering on Co is not spin dependent and we have no reason to believe otherwise for iron. Table 4.1 recapitulates the lifetimes measured for majority-spin and minority-spin image-potential-state electrons on Co and Fe.

	3 ML Fe/Cu(100)		6 ML Co/Cu(100)	
	majority	minority	majority	minority
τ_1	16 ± 2 fs	11 ± 2 fs	19 ± 2 fs	16 ± 2 fs
τ_2	54 ± 3 fs	43 ± 3 fs	71 ± 5 fs	58 ± 5 fs
τ_3	120 ± 10 fs	100 ± 10 fs	263 ± 15 fs	216 ± 15 fs

Table 4.1: Lifetimes τ_n determined for majority-spin and minority-spin image-potential-state electrons on 3 ML Fe/Cu(100) and 6 ML Co/Cu(100).

Finally we wish to comment on the contribution of phonons to the dynamics of image-potential states. We assume that electron-phonon scattering plays

only a very minor role in the dynamics of image-potential states on our ferromagnetic films. From temperature-dependent data of the (111) and (100) surfaces of Cu it is known that the interaction of image-potential-state electrons with phonons scales with the penetration of the wave function into the bulk. On the Cu(100) surface the contribution of phonon scattering to the image-potential-state linewidth at room temperature is below 1 meV [180]. The $n = 1$ image-potential state on the Cu(111) surface lies extremely close to the upper edge of the surface-projected band gap, and therefore the wave function has a very high overlap with the bulk states. At 90 K, where our measurements are carried out, the phonon contribution to the intrinsic linewidth of the $n = 1$ image-potential state is around 4 meV, i.e. less than 10% of the total intrinsic linewidth [92]. As it is unlikely that the image-potential states on the iron and cobalt films penetrate further into the bulk, this value constitutes an upper limit for the phonon-induced contribution to the linewidth.

4.3 Spin-resolved quantum beats

At sufficiently high photon energy, the image-potential states close to E_{vac} with higher quantum number n are also excited. Their energy separation is comparable to the bandwidth of the laser pulses and several image-potential states can be excited coherently [75]. After the excitation is over, the population of all coherently excited states develops (cf. Equation 4.3) according to

$$| \sum_n a_n(t)|^2 \quad = \quad \sum_n |a_n(0)|^2 e^{-\Gamma_n t} \tag{4.11}$$

$$+ \quad 2 \sum_{n \neq k} |a_n(0)||a_k(0)|e^{-(\frac{1}{2}\Gamma_n + \frac{1}{2}\Gamma_k + \Gamma^*_{nk})t} \cos((E_n - E_k)t/\hbar) \ .$$

A beating pattern is superimposed on the exponential decay of the image-potential state population $|a_n(0)|^2 e^{-\Gamma_n t}$. The interference term oscillates with the frequency $\omega_{nk} = (E_n - E_k)/\hbar$ corresponding to the energy difference between the coherently excited states. Thus quantum beat spectroscopy offers a unique experimental access to the image-potential states with a high quantum number which are otherwise far beyond the experimental energy resolution [75]. The amplitude of the oscillation decreases exponentially with the decay rates of the population $(\frac{1}{2}\Gamma_n + \frac{1}{2}\Gamma_k)$ as well as the dephasing between the participating states Γ^*_{nk}. Because the lifetime of the image-potential
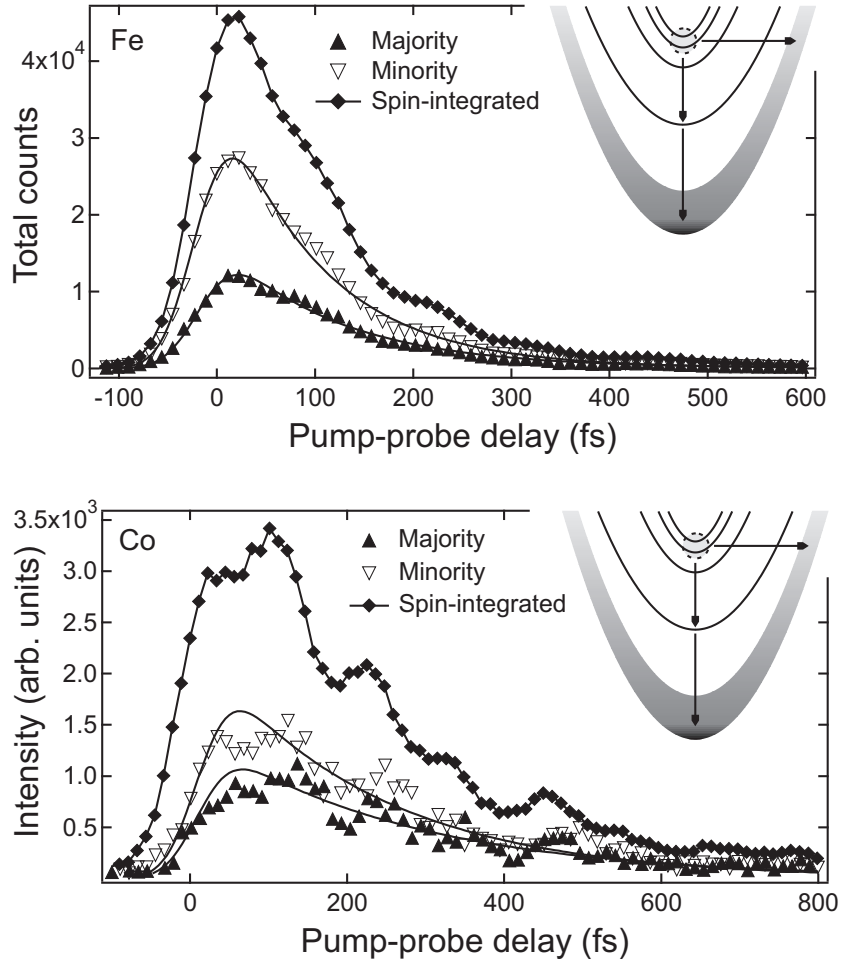
Figure 4.6: Time-resolved 2PPE spectrum of the coherently excited $n = 3$ and $n = 4$ image-potential state on Fe (upper panel, excitation energy $\hbar\omega_a = 4.84$ eV) and Co (lower panel, excitation energy $\hbar\omega_a = 4.79$ eV). Plotted are the spin-integrated (-♦-) trace as well as majority (▲) and minority (▽) electrons separately. The quantum-beat pattern is superimposed on the exponential decay of the $n = 3$ image-potential-state population (solid lines depict the population in the $n = 3$ calculated with optical Bloch equations). Note that the axis of ordinates has a linear scale in these graphs.

states scales with $\tau_n \propto n^3$, the decay of the quantum beats is dominated by the decay rate of the excited state with the lowest quantum number.

Figure 4.6 shows the time-resolved spectra of the coherently excited $n = 3$ and $n = 4$ image-potential states on iron and cobalt. The population in the $n = 3$ image-potential state lives $\tau_3^{\uparrow} = 120 \pm 10$ fs and $\tau_3^{\downarrow} = 100 \pm 10$ fs on iron while on cobalt $\tau_3^{\uparrow} = 263 \pm 15$ fs and $\tau_3^{\downarrow} = 216 \pm 15$ fs. From the measured beating frequency follows an energy difference of 30.5 ± 3 meV between the $n = 3$ and $n = 4$ image-potential state on iron and of 36 ± 3 meV between the $n = 3$ and $n = 4$ on cobalt. No spin dependence was found here, the results were identical for majority-spin, minority-spin and spin-integrated oscillations. As the exchange splitting of the $n = 3$ and $n = 4$ image-potential states is expected to scale with n^{-3}, and should thus be of the order of 2 meV, this value contributed to the error of this measurement.

Plotting only the oscillations (as done in Figure 4.7) reveals exponential decay of the amplitude. As a guide to the eye a cosine, oscillating with frequency $\omega = (E_3 - E_4)/\hbar$ and exponentially decaying $\propto \exp(-t/2\tau_3 - t/2\tau_4)$ was included. For the lifetime τ_4 of the $n = 4$ image-potential state $\tau_n \propto n^3$ was assumed. The oscillations of the minority-spin electrons on iron show a slightly stronger damping rate than strictly expected from population decay. As dephasing also contributes to the damping of the quantum beats, this may be a first indication that on iron also the dephasing rate is spin dependent. For the dotted grey line in the lower panel of Figure 4.7, which follows the minority-spin component of iron, an additional pure dephasing rate of $\hbar\Gamma_{34}^* = 2$ meV was assumed.

Assuming an n^{-3} dependence of the dephasing rate [56], this would correspond to a dephasing rate of 16 meV for the $n = 1$ image-potential state. To answer the question whether there is an additional dephasing rate, whether it truly affects minority-spin electrons stronger than majority-spin electrons and how good above estimate is, we have to venture deep into the next section, where we will revisit the energy-resolved measurements.

4.4 Energy-resolved measurements revisited

Let us begin this section with a look at Figure 4.8. The black traces represent a spin-resolved 2PPE spectrum of the $n = 1$ image-potential state on Fe recorded at zero pump-probe delay. A spectrum of the same state is displayed in grey on the right axis, this time though for 70 fs pump-probe delay. As the previous section dealt extensively with spin-dependent lifetimes, we can immediately identify the spin-dependent lifetimes as reason for the stronger
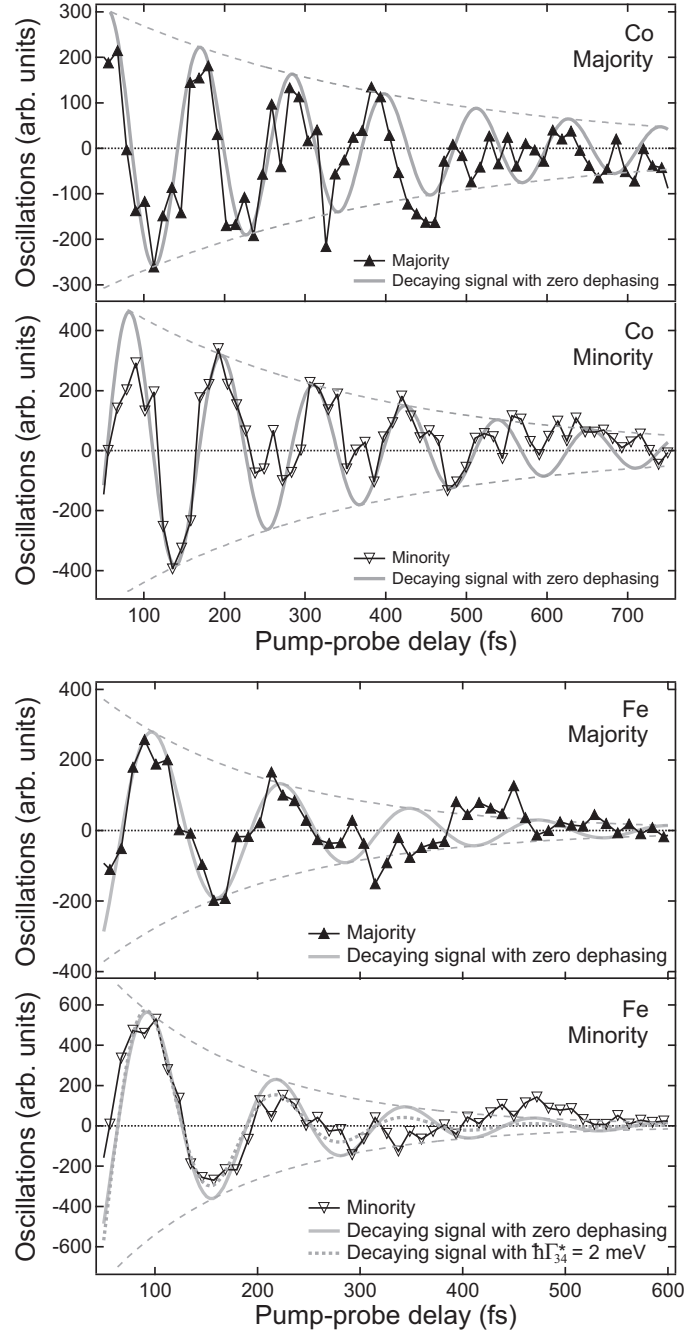
Figure 4.7: Quantum beats on cobalt (top) and iron (bottom), measured at the $n = 3$ energy. As a guide to the eye a cosine oscillating with frequency $\omega = (E_3 - E_4)/\hbar$ (solid grey line) and exponentially decaying $\propto \exp(-t/2\tau_3 - t/2\tau_4)$ (dashed grey line) was included. For the minority-spin component on iron an additional pure dephasing rate of $\hbar\Gamma_{34}^* = 2$ meV was assumed (dotted grey line).
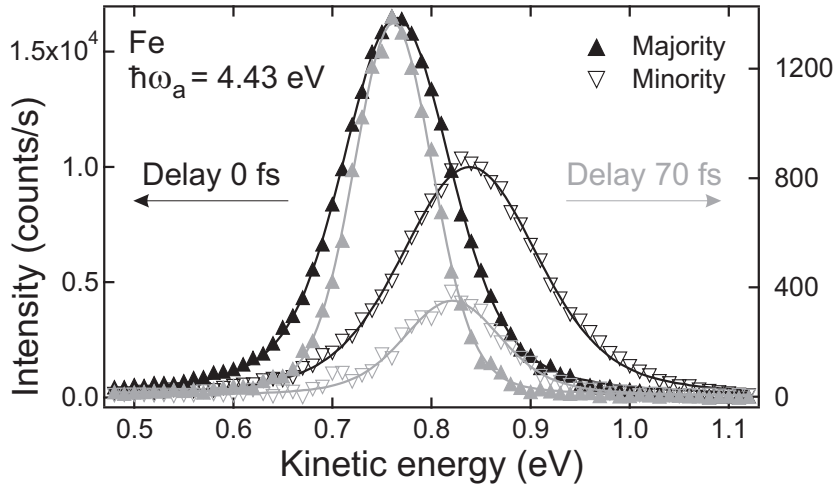
Figure 4.8: Spin-resolved spectrum of the $n = 1$ image-potential state on iron for zero delay between pump and probe pulse (black symbols and left axis) and for a pump-probe delay of 70 fs (grey symbols and right axis).

decrease of the minority-spin intensity compared to the majority-spin intensity. Without doubt the spin-dependent decay rate also contributes to the different linewidth observed in the majority and minority component.

Two further effects in Figure 4.8 attract attention. A noticeable shift of the peak positions occurs between the black and the grey traces and the linewidth decreases considerably in both spin channels. The underlying reasons will be discussed in this section.

4.4.1 Initial state effect

For a continuum of equally distributed initial states, the 2PPE spectrum reflects the density of the intermediate states. This is the case on the Cu(100) surface, for example. Here the excitation into the intermediate image-potential states takes place from the occupied sp bulk band, which has a near-constant density of states around the Fermi energy. The d bands are too far below E_F to participate in the excitation process. On the Cu(111) surface, on the other hand, the Shockley surface state lies only 0.435 eV below E_F [142] and a 2PPE spectrum of this surface exhibits an additional initial-state peak originating from the two-photon excitation of surface-state electrons. In a case where the pump-photon energy is close to the resonance energy between the Shockley surface state and the $n = 1$ image-potential state, the initial and the intermediate state peak can not be separated in the spectrum, and it may appear as if the $n = 1$ peak were asymmetric or merely
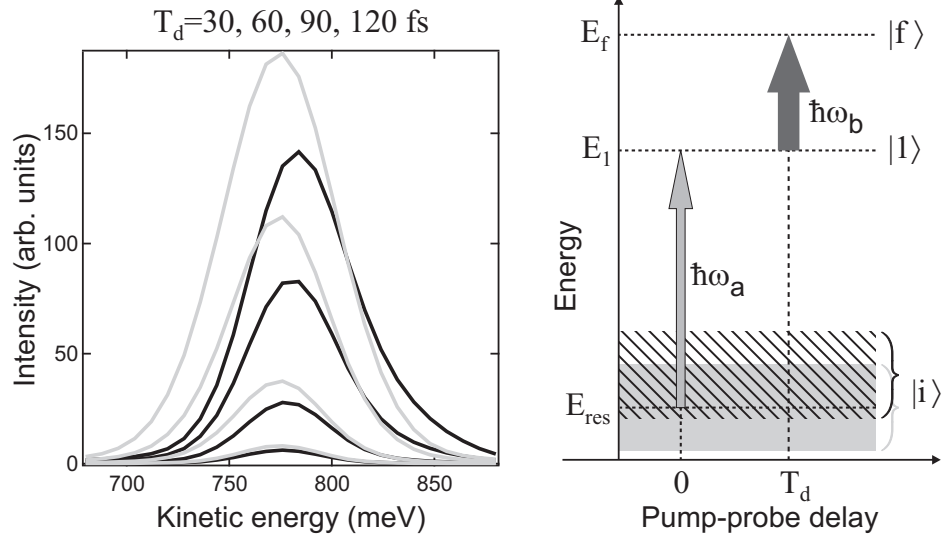
Figure 4.9: 2PPE spectra of a single intermediate state $|1\rangle$ excited from a narrow band of initial states $|i\rangle$ for increasing pump-probe delay from 30 fs (highest intensity) to 120 fs (lowest intensity). The grey traces constitute the spectra acquired with an initial state band (grey shaded area in the right hand side schematic) symmetric around the resonance energy $E_{\mathrm{res}} = E_1 - \hbar\omega_a$. The black traces obtained from an initial state band shifted to higher energies (hatched area) are noticeably shifted towards higher kinetic energies.

shifted in energy. Because the initial state peak can only be detected while pump and probe pulse overlap, the position of this peak seems to shift with increasing pump-probe delay towards the intermediate state energy.

For excitation from a narrow band, the effect is similar. To illustrate, I have simulated a 2PPE spectrum of a system of one intermediate state populated from a narrow band of initial states (100 meV wide) for increasing pump probe delay (30, 60, 90, and 120 fs from top to bottom in the left panel of Fig. 4.9). If the intermediate state is populated from a band symmetric around the resonance energy $E_{\mathrm{res}} = E_1 - \hbar\omega_a$, the intermediate state peak position remains unperturbed as a function of pump-probe delay. For excitation from an initial band shifted with reference to the resonance energy (in this simulation by 40 meV), the intermediate state peak will be influenced by the initial states and appear shifted in the 2PPE spectrum (at a pump-probe delay of 30 fs, the simulation yielded a peak shift of 12 meV). Only at large pump-probe delay, i.e. after the pump pulse is over, will the kinetic energy in both cases coincide. It is therefore essential to determine e.g. spin-dependent binding energies of the intermediate state, and the corresponding exchange
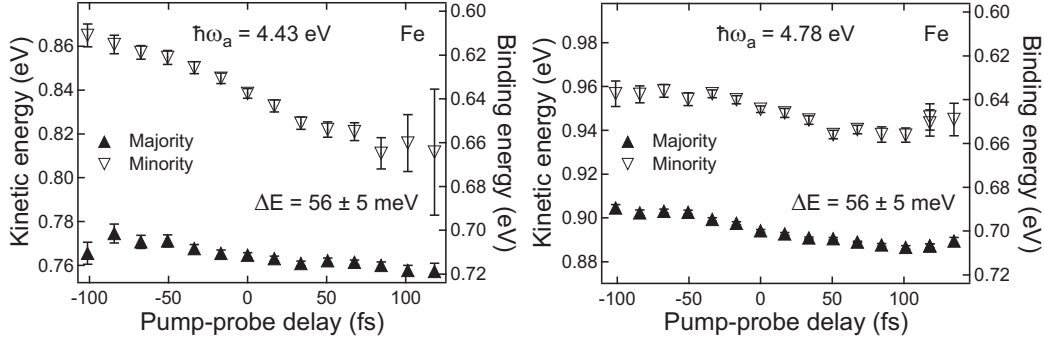
Figure 4.10: Kinetic energy of the $n = 1$ image-potential-state peak on iron as a function of pump-probe delay for two different photon energies. The binding energy of the intermediate state, and the exchange splitting ΔE, can be correctly derived only when the pump pulse is over.
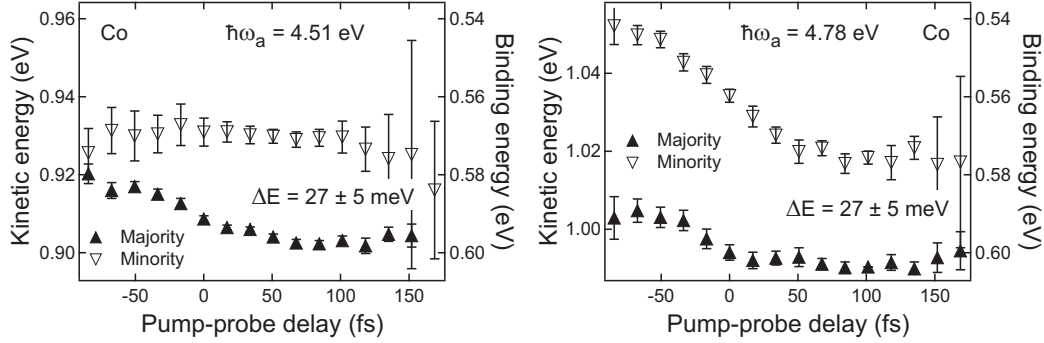

Figure 4.11: Measured kinetic energy of the $n = 1$ image-potential-state peak on cobalt as a function of pump-probe delay for two different photon energies. At large pump-probe delay the true binding energy of the $n = 1$ state can be determined.

splitting at large pump-probe delay only.

Figures 4.10 and 4.11 display the *measured* kinetic respectively binding energy of the majority- and minority-spin $n = 1$ image-potential state on iron and cobalt as a function of pump-probe delay for two different excitation energies. It becomes immediately evident that only after the pump pulse is over, the $n = 1$ peaks converge towards the true binding energy. Hence the exchange splitting ΔE can be correctly determined only at large pump-probe delay. For the exchange splitting given in Figures 4.10 and 4.11, all values for a pump-probe delay $T_d > 50$ fs, where the pump-pulse intensity has dropped below $1/e$ of the maximum intensity, have been averaged.

The rather large energetic shift of up to 40 meV of the minority-spin peak on cobalt indicates an excitation process from a narrow band or single ini-

tial state. It seems likely that the minority-spin surface resonance 0.45 eV below E_F participates in the excitation process. Though also the narrow d bands lie around E_F in our ferromagnetic films, the excitation probability is comparatively small from the d bands, given the totally symmetric s-like character of the image-potential-state wave function, and we do not expect a strong influence on the 2PPE spectrum.

Band structure calculations for thin iron films yield controversial results as to whether the minimum of the minority-spin Δ_1 band lies below the Fermi level (cf. Fig. 3.4) [30]. The fact that we can excite minority-spin electrons into the image-potential states at all is a strong indication that the sp band indeed reaches below E_F. The strong peak shift in the minority-spin channel for low excitation energy only confirms this.

In the last chapter, we have already extensively discussed the role of the initial state in the spin polarisation of the image-potential-state population. In our further analysis we will also have to bear in mind that the initial states affect the intermediate-state-peak position and lineshape, which will consequently both vary with pump-probe delay.

	3 ML Fe/Cu(100)		6 ML Co/Cu(100)	
	majority	minority	majority	minority
E_1	714 ± 4 meV	658 ± 7 meV	600 ± 8 meV	573 ± 8 meV
ΔE_1	56 ± 5 meV		27 ± 5 meV	
E_2	201 ± 4 meV	194 ± 7 meV	166 ± 8 meV	160 ± 8 meV
ΔE_2	7 ± 3 meV		6 ± 3 meV	
Φ	4.75 ± 0.02 eV		4.73 ± 0.02 eV	

Table 4.2: Binding energies E_1 and E_2, exchange splitting ΔE_1 and ΔE_2 determined for majority-spin and minority-spin image-potential states on 3 ML Fe/Cu(100) and 6 ML Co/Cu(100). The work function Φ at 90 K for the two magnetic films is also given.

To conclude this chapter, in Table 4.2 we have combined the binding energies and exchange splittings obtained in our experiments for iron and cobalt thin films.

4.4.2   Spin-dependent dephasing

A glance at Figure 4.12 shows that with increasing time-delay between pump and probe pulse the linewidth of the majority- and minority-spin $n = 1$ image-potential state decreases. A closer look reveals also a change in lineshape. The image-potential state peaks develop from a Lorentzian with large
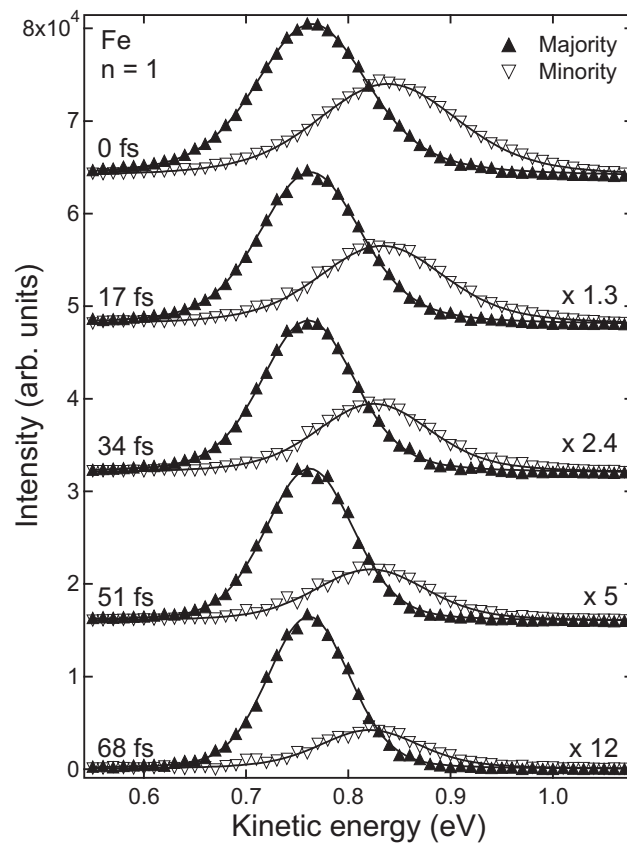
Figure 4.12: Energy- and spin-resolved 2PPE spectra of the $n = 1$ image-potential state for increasing pump-probe delay; the spectra are normalised on the majority-spin channel at 0 fs, the numbers on the right indicate the multiplication factors of the intensity.

wings on both sides to a Gaussian form. Hence, it becomes evident that, unlike in conventional photoemission, where the linewidth (full width at half maximum, FWHM) $\hbar\Gamma$ is given by the lifetime τ and the dephasing rate Γ^* of the photohole as

$$\hbar\Gamma = \hbar/\tau + 2\hbar\Gamma^* \; , \tag{4.12}$$

in two-photon photoemission the pump-probe delay enters into the equation as well. This is of course unsurprising, as in two-photon photoemission the probe pulse samples a transient population of the intermediate state. Unfortunately, the 2PPE linewidth as function of pump-probe delay depends also on the shape of the laser pulses.

In a detailed analytical and numerical analysis, Boger and coworkers found the following behaviour of the linewidth for Gaussian laser pulses upon off-resonant excitation from a discrete initial state, i.e. when the initial and intermediate state peak in the spectrum are separated [24].

The lineshape of the intermediate state in 2PPE is a convolution of a Gaussian function, which is determined by the experimental resolution (i.e. the energy resolution of the electron analyser and the bandwidth of the probe pulse), with a Lorentzian curve whose width depends on pump-probe delay. For increasingly negative delay, where the probe pulse precedes the pump pulse, photoemission is mainly caused by the overlap of the pulse tails and the Lorentzian width increases linearly with decreasing delay. The pump- and probe-pulse duration determine the slope. An offset between two curves for large negative delay corresponds to the difference in decay rates.

In the limit of separated pump and probe pulses, i.e. when the pump process is over and the population ρ_{nn} decays exponentially $\rho_{nn}(t) \propto \exp(-\Gamma_n t)$, the decay rate Γ_n does not contribute to the linewidth. Here the linewidth is solely given by a convolution of the experimental resolution with twice the pure dephasing rate Γ^*.

Without dephasing, the photoemission signal equals a convolution of the Gaussian probe pulse with an exponential function. This yields a Gaussian, shifted, but not broadened. Thus at large delay only the dephasing rate $2\Gamma^*$ but not the lifetime contributes to the measured linewidth. Moreover, when the pump pulse is over, details of the excitation process such as the density of initial states do not influence the measured linewidth. Hence we are provided with an excellent possibility to measure the dephasing rate [152].

The same behaviour is found for excitation from a continuum of initial states [22]. This model describes the excitation process from sp bands into the image-potential states on the Cu(100) surface rather well, which is nicely demonstrated by the concordance between experiment and theory [23]. As

no initial state peak appears in the spectrum when pump and probe pulse are separated, the result for the limit of large pump-probe delay is also valid for *resonantly* excited intermediate states or states excited from a narrow band.

In Figures 4.13 and 4.14, the linewidth (full width at half maximum, FWHM) of the majority and minority component of the $n = 1$ image-potential state as a function of pump-probe delay is compared for a 3 ML and a 4 ML iron film. In the hope of minimising the initial-state effect, the measurements have also been carried out at higher photon energies, though here the curves deviate strongly from the behaviour described above[4]. At increasingly negative delay, the linewidths saturate rather than increase linearly, and the traces do not converge as expected in the limit of separated pulses. The upwards slope at large positive delay in the curves with higher excitation energy can be attributed to interband scattering from the higher image-potential states [22]. It is difficult to pinpoint the reason for the decreasing slope at negative delay. We can not rule out influences of the initial states, and bulk or surface states above the Fermi energy, which are pumped with the IR pulse and probed with the UV pulse, might also entail such a behaviour.

Though the initial-state effect renders a quantitative analysis of the FWHM over the full range of pump-probe delay impossible, the influence of the pump pulse (and hence the initial state) is negligible at sufficiently large pump-probe delay. If we excite only the $n = 1$ image-potential state, interband scattering will also not interfere. We will therefore concentrate on the linewidth traces at high delay measured with low photon energy.

Let us first consider the results in Figure 4.13. The experimental resolution, i.e. energy resolution of the analyser and probe pulse bandwidth, is of course identical for both majority and minority electrons. Hence the clear difference in linewidth for spin-up and spin-down indicates a spin-dependent dephasing rate $\Gamma_{1f}^{*\uparrow} < \Gamma_{1f}^{*\downarrow}$.

On the cobalt film, on the other hand, the difference in linewidth at large

---

[4]It should be noted here that several reasons point towards Gaussian shaped laser pulses in our experiment. First, the linewidth vs. pump-probe delay measurement was also carried out for the $n = 1$ image-potential state on Cu(100) (not shown), where the influence of the initial states is weak and no deconvolution of the data into spin channels is necessary. There the FWHM trace behaved as expected for Gaussian pulses. Second, a reconstruction of the IR laser pulses from the autocorrelation function (as described in [22]) also yielded a Gaussian rather than hyperbolic secant pulse shape. Third, the majority and minority linewidth traces for the cobalt films converge at large pump-probe delay. For other laser pulse shapes like hyperbolic secant or cosine, the lifetime enters into the linewidth in the limit of separated pulses [24]. We know, however, that majority- and minority-spin electrons on cobalt films do not have the same lifetime and therefore
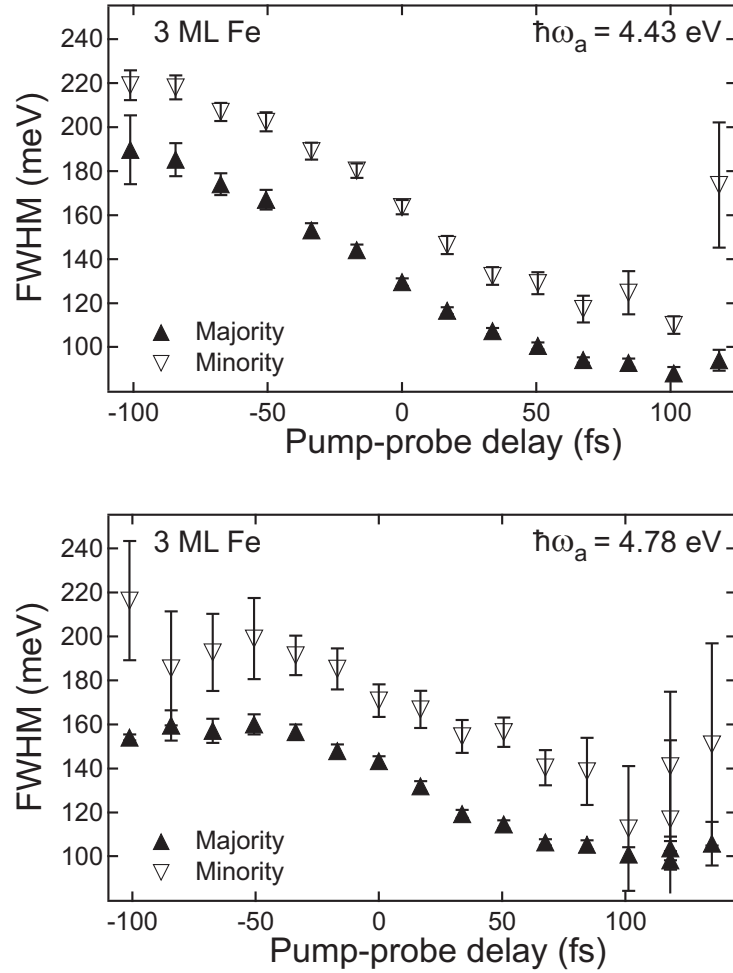
Figure 4.13: Full width at half maximum (FWHM) of the majority and minority component of the $n = 1$ image-potential state on a 3 ML iron film as a function of pump-probe delay. The measurements were carried out with a photon energy of $\hbar\omega_a = 4.43$ eV (top) and $\hbar\omega_a = 4.78$ eV (bottom). In the latter case the $n = 2$ state was also populated and interband scattering took place.
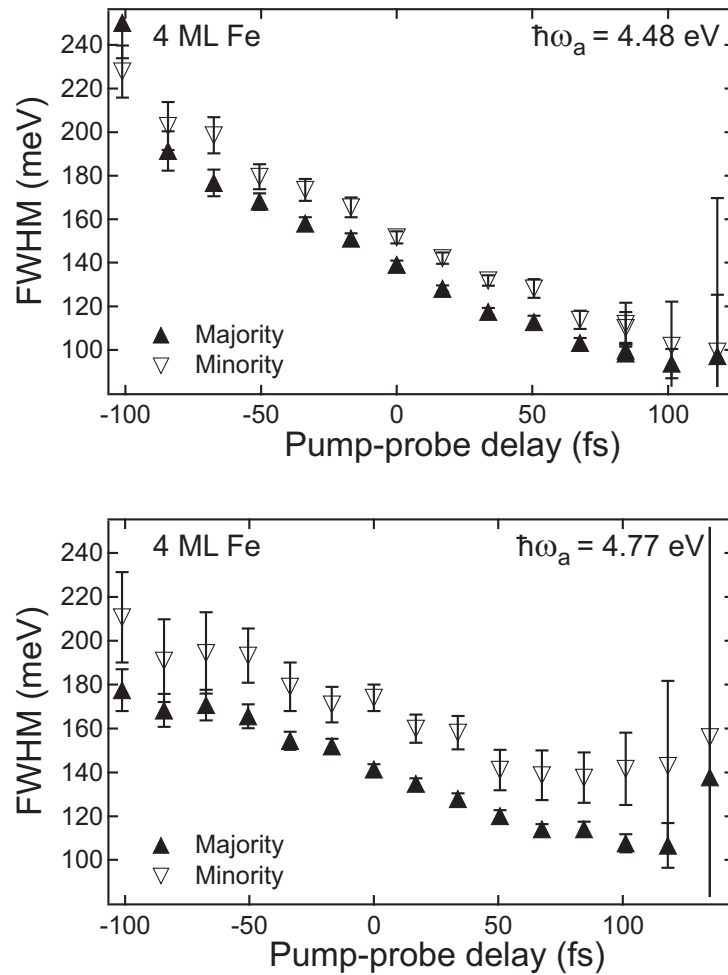
Figure 4.14: Full width at half maximum (FWHM) of the majority and minority component of the $n = 1$ image-potential state as a function of pump-probe delay. The measurements were carried out on a 4 ML iron film with a photon energy of $\hbar\omega_a = 4.48$ eV (top graph) and $\hbar\omega_a = 4.77$ eV (bottom graph). In the latter case the $n = 2$ state was also populated and interband scattering took place.
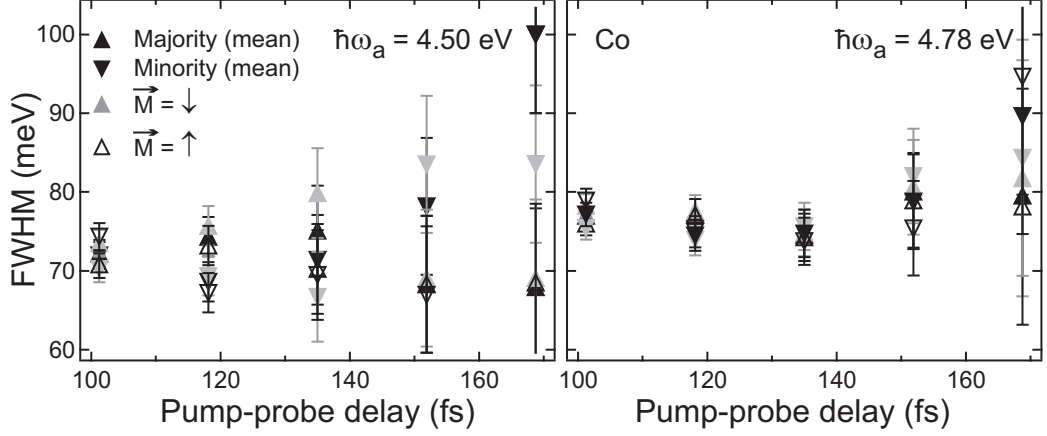
Figure 4.15: The linewidth on cobalt is not spin dependent at large pump-probe delay within the error. Grey and open symbols depict the values obtained from the spectra for the two antiparallel directions of magnetisation as indicated (cf. Sec. 3.6), while for the black symbols the dichroic spectra were averaged. Obviously on cobalt no spin-dependent dephasing is found.

delay is below the statistical error (cf. Fig. 4.15).

The following side note might be of interest here: Because our partial spectra must be deconvoluted from the measured data as discussed in Section 2.2, the majority and minority component are not independent and an error in the Sherman function could very well affect the lineshape. But only with a smaller Sherman function would the difference between majority and minority linewidth decrease and we have already excluded a Sherman function $S \leq 0.22$.

To further confirm that there truly is a spin-dependent dephasing rate on iron films, energy-resolved spectra measured with two different photon energies at zero delay were compared with a simulation employing the optical Bloch equations (cf. Fig. 4.16). In the simulations an analyser resolution of 70 meV was assumed, which gives a total energy resolution of 83 meV in combination with the probe-pulse width of 45 meV. The lifetimes $\tau_{1,2}^{\uparrow;\downarrow}$ of the $n = 1$ and the $n = 2$ image-potential state have been independently gathered from the time-resolved measurements. The pulse length of the probe pulse was determined from the interferometric autocorrelation and a cross-correlation measurement of the Shockley surface state on Cu(111) provided the pump pulse length and the time "zero" of the pump-probe delay. Both spectra were simulated with a spin-dependent dephasing rate, for the spectra acquired with low photon

---

we must conclude that the shape of our laser pulses is indeed Gaussian.
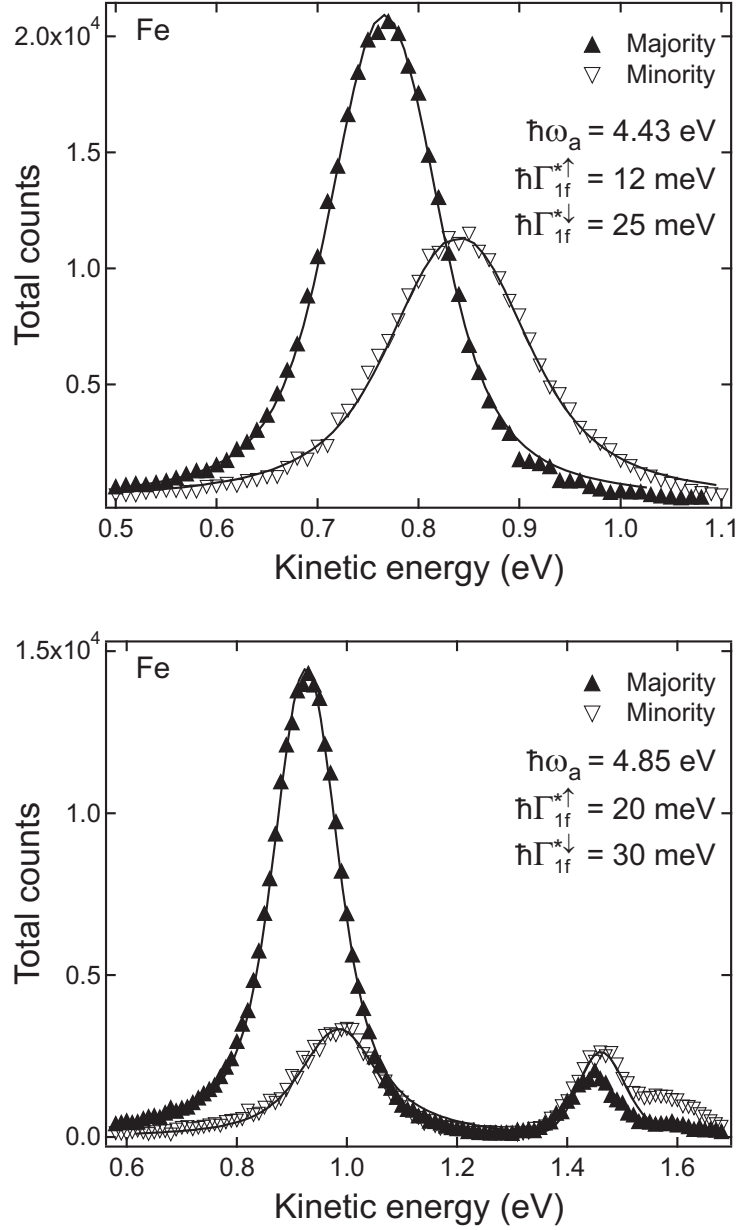
Figure 4.16: A spin- and energy-resolved spectrum (symbols) of the $n = 1$ and $n = 2$ image-potential state on iron is simulated with Bloch equations (solid line). In the upper panel a dephasing rate of $\hbar\Gamma_{1f}^{*\downarrow} = 25$ meV for the minority and $\hbar\Gamma_{1f}^{*\uparrow} = 12$ meV for the majority electrons was employed, while the simulation in the lower panel was done with $\hbar\Gamma_{1f}^{*\downarrow} = 30$ meV and $\hbar\Gamma_{1f}^{*\uparrow} = 20$ meV.
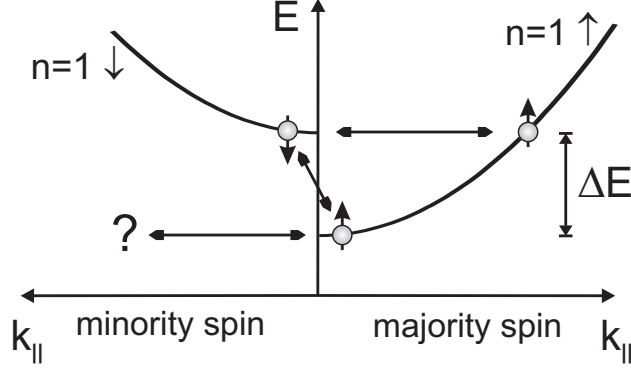
Figure 4.17: Schematic of the free-electron like dispersion parallel to the surface of the majority and minority $n = 1$ band. A possible magnon-scattering induced elastic process (horizontal) is indicated, as well as a spin-flip process (vertical), where energy on the order of the exchange splitting is exchanged.

energies $\hbar\Gamma^{*\downarrow}_{1f} = 25$ meV and $\hbar\Gamma^{*\uparrow}_{1f} = 12$ meV was employed, while I used $\hbar\Gamma^{*\downarrow}_{1f} = 30$ meV and $\hbar\Gamma^{*\uparrow}_{1f} = 20$ meV for the high photon energy spectra. The slightly higher dephasing rates for $\hbar\omega_a = 4.78$ eV are probably due to interband scattering from the $n \geq 2$ states into the $n = 1$ image-potential state.

It is difficult to decide how well the dephasing rate is actually quantifiable in our system, but the rather good conformance of the simulations with our measurement add credit to our linewidth measurement and we must conclude that we indeed observe spin-dependent dephasing processes.

Scattering events which change the energy and/or momentum of an electron on a scale smaller than the experimental resolution, i.e. leave the detectable population unchanged, but nevertheless destroy the phase coherence between intermediate and final state, are the origin of pure dephasing. The main causes of "quasi-elastic" scattering, at least on the surface of a paramagnet, are phonon and defect scattering. While we have already ruled out phonons as a source for a large contribution to the linewidth, defects have been shown to cause quasi-elastic scattering within one image-potential state [23]. It seems unlikely that defect scattering is spin dependent on the iron film, while it is clearly not on cobalt. However, we can not determine the scattering process behind the spin-dependent dephasing in an unambiguous manner.

We interpret the spin-dependent dephasing in terms of electron-magnon scattering on the iron surface. Acoustic magnons follow a quadratic dispersion $E(q) = Dq^2$, with an exchange stiffness D of $230 - 290$ meVÅ^2 in bulk iron (spin waves in thin films are usually slightly softer) [170]. Hence an acoustic

spin wave in iron is of around 3 meV in energy for the necessary momentum transfer between the minority and majority band, an energy scale which definitely qualifies as quasi-elastic for our energy resolution. This process is indicated schematically in Figure 4.17 by the horizontal double-headed arrow. Note that the image-potential band is approximately a two-dimensional paraboloid, which significantly extends the phase space for electron scattering.

A scattering process between the two spin bands necessarily involves a spin flip. Spin-flip scattering from minority- to majority-spin states corresponds to the emission of a magnon, while spin-wave absorption satisfies angular-momentum conservation when scattering occurs from majority-spin into minority-spin states.

From the minimum of the minority-spin band, an electron can easily scatter into the majority-spin band via the emission of a magnon. Though at a sample temperature of 90 K low-energy magnons may be already excited and in principle also a majority-spin electron could absorb a magnon and scatter into a minority-spin band, this is impossible at the minimum of the majority-spin image-potential band. Here, the majority-spin electron simply lacks a corresponding minority-spin image-potential state to scatter into, as is indicated by the question mark in Figure 4.17. We have thus identified a definitely spin-dependent quasi-elastic scattering process as a probable source for the spin-dependent dephasing rate of the $n = 1$ image-potential state in iron. As we will encounter magnon scattering again, we will resume the discussion of this topic in the next sections.

The reader may have noticed that the linewidth at large pump-probe delay on the 4 ML iron film differs not as much as it does on the 3 ML iron film. The absolute linewidth, however, is slightly larger for 4 ML. A time-resolved measurement on 4 ML iron yields exactly the same lifetimes as on 3 ML, namely $\tau_1^\uparrow = 16$ fs and $\tau_1^\downarrow = 11$ fs. The defect density on the 4 ML film should be small compared with 3 ML (investigations with ion beam triangulation [13] indicate a less distorted film at a coverage of 4 ML), and defect scattering will not add to the linewidth. The smaller distortion of the 4 ML film also leads to a higher coercitivity. Therefore the 2PPE measurements were carried out at a sample temperature of 230 K rather than at 90 K and phonon scattering may already be significant. It is also more difficult to determine the linewidth on the 4 ML film, as the background from direct photoemission of thermally excited electrons is already noticeable at these temperatures. What is more, with an exchange splitting of only 40 meV, the 4 ML film might be closer to the Curie temperature, where the asymmetry between spin wave absorption
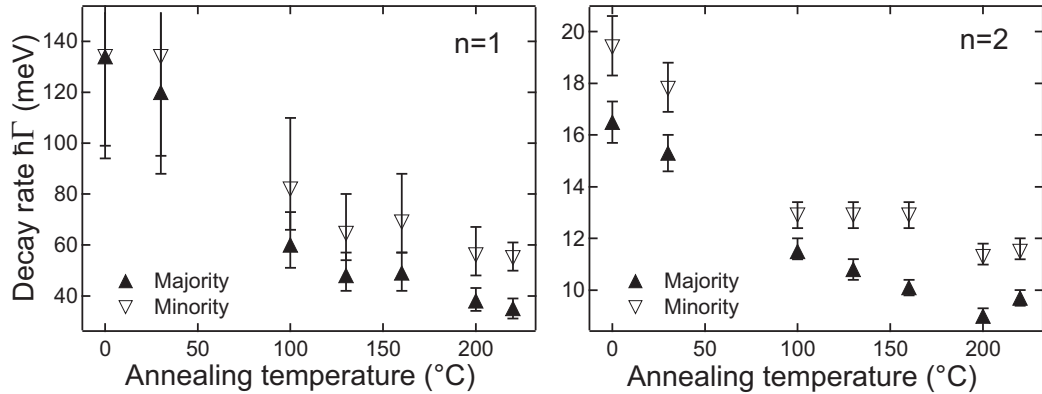
Figure 4.18: Spin-dependent decay rates of the first (left hand side) and second (right hand side) image-potential state as a function of increasing annealing temperature (and thus decreasing defect density).

and emission is smaller.

A further explanation for the different behaviour of the 3 and 4 ML films might be provided by scattering off standing spin waves (schematically depicted in Fig. 4.17). In a theoretical paper on spin dynamics of ultrathin Fe(100) films, Tang and coworkers calculate a standing spin-wave mode ($\mathbf{q}_\parallel = 0$) in ultrathin bcc Fe(100) films, whose energy scales inversely with the number of layers $\propto N^{-2}$ [170]. For 4 ML bcc iron the lowest lying standing spin wave mode has an energy of 60 meV, while for a thinner film an even higher energy is expected. In a more recent theoretical paper, where the influence of a W(110) substrate is considered, the 3 ML bcc iron film exhibits a 60 meV standing magnon with a strong amplitude in the surface layer, where image-potential states have a high probability density [39]. For the 4 ML film the energy of the lowest lying standing magnon mode was calculated to be around 35 meV. Accordingly the interaction strength of the image-potential-state electrons with such a standing spin wave may be determined by how well the magnon energy corresponds to the exchange splitting between the majority and minority $n = 1$ band.

4.5   Defect scattering on cobalt

As already discussed in the last section, on cobalt the linewidth measurements show not the difference between majority- and minority-spin electrons they display on iron. One might argue that defect scattering could nevertheless be a source for the quasi-elastic spin-dependent scattering process on
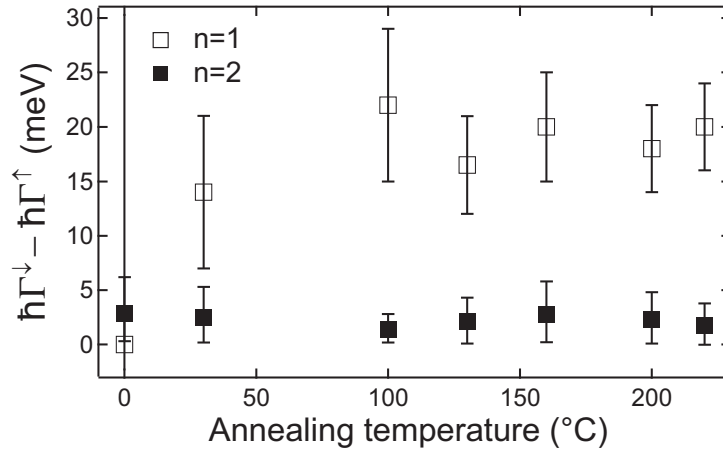
Figure 4.19: The difference between majority and minority decay rate remains constant upon decreasing defect density (increasing annealing temperature). With a spin-dependent defect scattering rate this difference would increase or decrease.

iron, because the annealed cobalt film is very smooth and rather shows no defect scattering at all. However, on cobalt, defect scattering shows no sign of spin dependence, which can be seen as follows.

Usually the cobalt films were evaporated with the substrate cooled to liquid nitrogen temperature and subsequent annealing to 210°C ensured a smooth surface[5]. This method of preparation provides a perfect opportunity to gain information about defect scattering, since the defect density can be varied simply by annealing to higher or lower temperatures. Image-potential states become discernible in the energy-resolved spectra starting at annealing temperatures of around $10 - 30$°C. Increasing the annealing temperature leads to narrower image-potential state peaks with higher intensities and longer electron lifetimes in the image-potential states. This has been quantified in Figure 4.18, where the decay rate $\hbar\Gamma = \hbar/\tau$ of the first and second image-potential-state population is shown for increasing annealing temperature.

Let us assume that at high annealing temperatures the surface is smooth, little to no defect induced scattering occurs and all other decay processes are included in the (spin-dependent) decay rate $\Gamma^{\uparrow\downarrow}(T = 210$°C$)$. As defects

---

[5]At higher annealing temperatures Cu diffuses to the top of the Co film due to the formation of pinholes [149]. For iron films such annealing experiments are not possible, because the onset temperature for diffusion of substrate atoms to the surface is not far above room temperature [109].
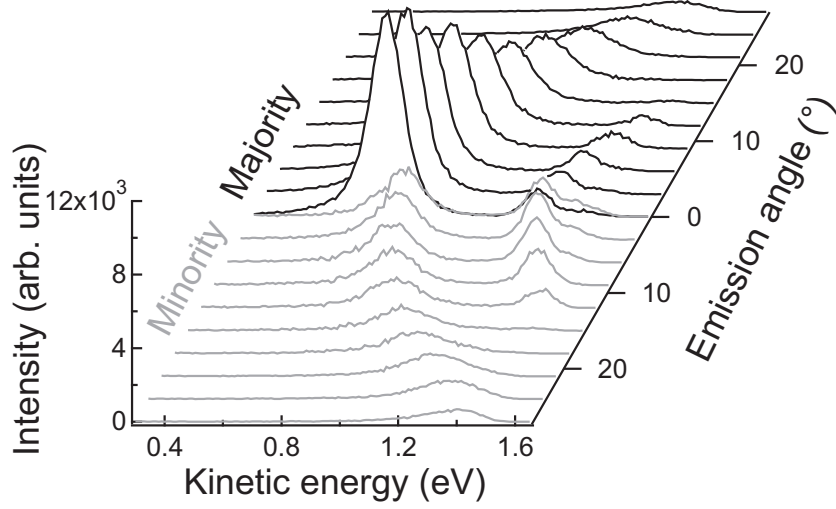
Figure 4.20: Energy-resolved 2PPE spectra of the first and second image-potential state for increasing emission angle. The majority-spin component is displayed in black, minority in grey.

cause elastic decay into the bulk [25], the decay rate

$$\Gamma^{\uparrow\downarrow}(T) = \Gamma^{\uparrow\downarrow}(T = 210°C) + \rho(T)\Gamma^{\uparrow\downarrow}_{\text{defect}} \tag{4.13}$$

increases for lower annealing temperatures T, i.e. increasing defect density $\rho(T)$. With a spin-dependent defect scattering rate $\Gamma^{\uparrow\downarrow}_{\text{defect}}$, the difference between the majority and minority decay rate $\Gamma^{\uparrow\downarrow}(T)$ must change with T. As Figure 4.19 indicates, this is not the case especially for higher annealing temperature, where the determination of the decay rate is more reliable due to the overall larger lifetimes. We must therefore conclude that defect scattering (off the rough surface) on Co is not spin dependent.

4.6   Conquering k-space

Up to now we have discussed solely measurements where the emitted photoelectrons were detected normal to the sample surface. Upon varying the detection angle we have access to the electronic states with nonzero parallel momentum. Figure 4.20 displays energy-resolved spectra of the majority and minority component of the first and second image-potential state for various electron emission-angles relative to the surface normal. For such a measurement the excitation energy $\hbar\omega_a$ is tuned as close as possible to the work function in order to occupy the image-potential band up to the vacuum energy, while at the same time avoiding direct photoemission and thus

space-charge effects. Because the momentum of the electron parallel to the surface is conserved in the photoemission process, $k_\parallel$ can be calculated from the emission angle ϑ and the kinetic energy as[6]

$$k_\parallel = \sin \vartheta \sqrt{\frac{2m_e E_{\text{kin}}}{\hbar^2}} \ . \tag{4.14}$$

We are thus able to observe the dispersion $E(k_\parallel)$ of the image-potential state energies with parallel momentum $k_\parallel$ almost up to the kinetic energy corresponding to $\hbar\omega_b$. Here the image-potential state is not fully excited anymore, as the cut-off image-potential-state peak in the outermost traces of Figure 4.20 indicates. We can also estimate an effective mass

$$\frac{1}{m^*} = \frac{m_e}{\hbar^2} \frac{d^2 E(k_\parallel)}{dk_\parallel^2} \tag{4.15}$$

in units of the free electron mass m_e for the $n = 1$ image-potential state, though our rather large angular resolution of $\Delta\vartheta = \pm 2.5°$ prevents a rigid determination of the spin dependence of the effective mass. With $m^*_{\text{Co}} = 0.64 \pm 0.14$ on the cobalt film and $m^*_{\text{Fe}} = 0.55 \pm 0.15$ on the iron film, the effective masses on the ferromagnets are small compared with the effective mass of $m^*_{\text{Cu}} = 0.8 \pm 0.1$ of the $n = 1$ image-potential state on the Cu(100) surface [180]. A surface state with an energy close to the lower border of the surface-projected band gap is in fact expected to have a rather low effective mass [66]. From the band structure of Cu(100) and the two magnetic pseudo-morphs [105], we can indeed assume that the image-potential states on iron and cobalt lie closer to the lower border of the band gap. The smaller effective mass on iron is even consistent with the fact that the image-potential states on iron are closer to the lower border than on cobalt.

4.6.1 Spin-dependent resonant interband scattering

Following the dynamics of the image-potential-state electrons along the dispersing $n = 1$ band, a strong refilling process from a state with a longer lifetime can be observed in the majority component, once the energy is resonant with the minimum of the $n = 2$ image-potential band. Such a refilling process has been successfully identified as defect-induced resonant interband scattering from the $n = 2$ into the $n = 1$ image-potential state on the Cu(100) surface [15, 26]. Defects have been shown to cause (quasi-)elastic scattering

---

[6]The emission angle ϑ is measured with respect to the surface normal. Hence $k_\parallel = 0$ for normal emission.

with a comparatively large momentum transfer not only between image-potential states, but from image-potential states into the bulk as well [25]. Here, however, we are confronted with a *spin-dependent* quasi-elastic scattering process. Figure 4.21 shows a time-resolved 2PPE measurement for both spin channels at an energy 120 meV and 130 meV below, and in resonance with, the minimum of the respective $n = 2$ image-potential band. Obviously nothing changes in the minority-spin channel, while the majority-spin trace features a much stronger refilling component once measured in resonance with the $n = 2$. The increase of interband scattering manifests in a shift of the inflexion point of the biexponential decay towards an earlier point in time. In the majority channel the decay rate of the $n = 2$ image-potential state dominates the overall decay of the $n = 1$ image-potential-state population already at smaller pump-probe delay. No such effect was found on cobalt, but here the interband scattering rate is admittedly overall much lower and a similar effect might be obscured by the background.

To ascertain that the interband scattering rate on iron is indeed spin-dependent, and not merely an effect of spin-dependent excitation strengths, the spin- and energy-resolved 2PPE spectrum in Figure 4.22 was simulated using the optical Bloch equations with the same procedure as in Section 4.4.2 (Though here the spectrum was measured with an incidence angle of 45°, which mimics the excitation geometry encountered in the measurements for Figure 4.21). Accordingly, the simulation employed a pure dephasing rate of $\Gamma_{1f}^* = 20$ meV and $\Gamma_{1f}^* = 30$ meV for majority- and minority-spin electrons, respectively. In References [75, 131, 91, 22] it is assumed that the optical matrix elements, and hence the excitation strengths, scale according to

$$M_{ni} \propto M_{fn} \propto n^{-3/2} \ . \tag{4.16}$$

From the considerations of Section 4.4.1 and the almost equal minority-spin intensity in the $n = 1$ and the $n = 2$ image-potential state in the iron spectrum of Figure 3.3, it becomes immediately clear that the strong participation of narrow bands in the excitation process renders this assumption not applicable in our systems. Only for the probe process, where the occupied bulk electronic states play no role, we may safely employ this $n^{-3/2}$ dependence. The relative excitation strengths $|M_{1i}^{\uparrow}|/|M_{2i}^{\uparrow}| = 1/0.47$ and $|M_{1i}^{\downarrow}|/|M_{2i}^{\downarrow}| = 1/0.85$ between $n = 1$ and $n = 2$ image-potential state were estimated from the simulation of the spectrum. Qualitatively, this result could be anticipated from the pronounced intensity of the minority-spin $n = 2$ image-potential state in Figure 4.22. Therefore considering only population, we would expect the interband scattering to dominate the minority channel. As evident
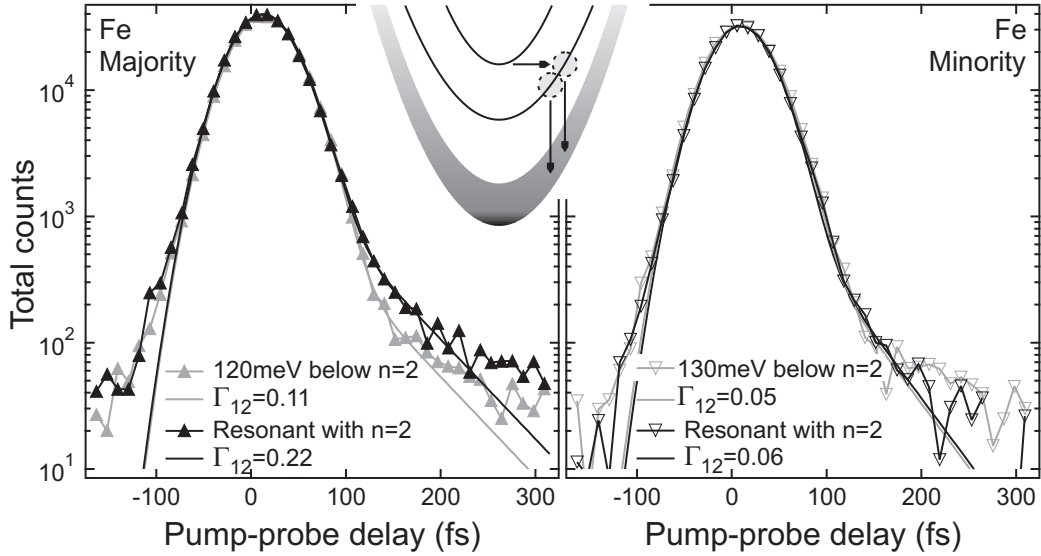
Figure 4.21: Majority (left) and minority-spin (right) traces of a time-resolved 2PPE measurement at off-normal emission. Kinetic energy and emission angle ϑ were chosen such that the transient population in the $n = 1$ state was probed, in resonance with the minimum of the $n = 2$ image-potential band (black) and for comparison $120 - 130$ meV below the resonance (grey) for both spin channels respectively. In the experiment this corresponded to time-resolved measurements at $\vartheta = 25.5°$ vs $\vartheta = 22°$ for the majority-spin electrons and $\vartheta = 22°$ vs $\vartheta = 18°$ for the minority-spin electrons. The two points in k-space are indicated by the dashed circles in the schematic inset. The simulation (solid lines) was done with optical Bloch equations, using matrix elements obtained from a simulation of the energy-resolved spectra in Fig. 4.22. Note that the deviation of the simulation from the measured data at large pump-probe delay is due to the small background intensity of the measurement.
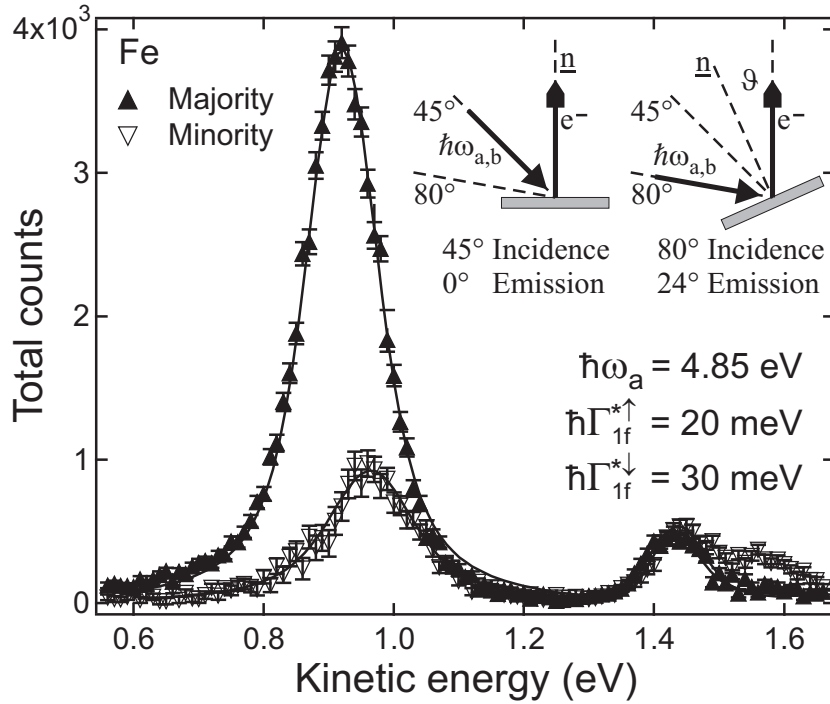
Figure 4.22: For an educated estimation of the interband scattering rate Γ_{12} with optical Bloch equations, the relative excitation probabilities for majority and minority electrons in the $n = 2$ state were determined by simulating this spin-resolved spectrum, which was measured in normal emission but with an incident angle of 45°. This excitation geometry is similar to the one in Fig. 4.21, where the emission angle ϑ relative to the surface normal $\underline{n}$ determines the angle of the incident light as $10° + \vartheta$ for excitation through the 80° window (schematically shown in the inset).

from Figure 4.21, the opposite is the case. It could be derived from our simulations that not only is the majority interband transition rate with $\Gamma_{12}^{\uparrow} = 0.11$ higher than the minority rate with $\Gamma_{12}^{\downarrow} = 0.05$, but also only the majority rate doubles to $\Gamma_{12}^{\uparrow} = 0.22$ at energetic resonance with the $n = 2$ band.

It should be kept in mind that the simulation is done for each spin channel separately. This corresponds to a strict spin-conservation, i.e. no electron is permitted a spin flip. However, a spin-flip process from the minority $n = 2$ into the majority $n = 1$ image-potential state accompanied by the emission of a magnon can not be excluded. Only the fact that more electrons are scattered *into* the majority-spin $n = 1$ can be safely deduced from the measurement, there is no way of telling where they come from. In principle, if we were to observe a long-living component in the biexponential trace of the majority-spin $n = 1$ image-potential state with the characteristic lifetime of the minority-spin $n = 2$ image-potential state, we had the ultimate proof of spin-flip scattering. Unfortunately the signal-to-background ratio at a pump-probe delay of $150 - 200$ fs is too low to determine the characteristic timescale of the long-living component accurately enough[7].

As defect scattering[8] has been identified as the cause of resonant interband scattering before [15], and has now been established as a spin-independent process, we are actually surprised that although much more minority-spin electrons are excited into the $n = 2$ image-potential state, no significant resonant refilling process is detected in the minority-spin $n = 1$ image-potential state. Were we to assume for one moment that the defect scattering rate were spin dependent, and larger for minority-spin electrons, as one might also deduce from the larger minority dephasing rate introduced in Section 4.4.2, we expected also a much lager (defect-induced) interband scattering rate in the minority-spin channel. This is clearly not the case here.

Electron-magnon scattering, on the other hand, is accompanied by a spin-flip. Minority-spin electrons could scatter almost resonantly from the $n = 2$ image-potential state into the majority-spin $n = 1$ image-potential state via the emission of an acoustic magnon. As a rather large momentum transfer of approximately $q = 0.2$ Å^{-1} is required, a corresponding acoustic magnon would have an energy of around 10 meV. At a sample temperature of 90 K, such a magnon is not readily available for absorption, and electron-magnon

---

[7]Substraction of a background (which was not done here) in such experiments can far too easily distort the measurement and lead to wrong assumptions, especially if the data is viewed on a logarithmic scale.

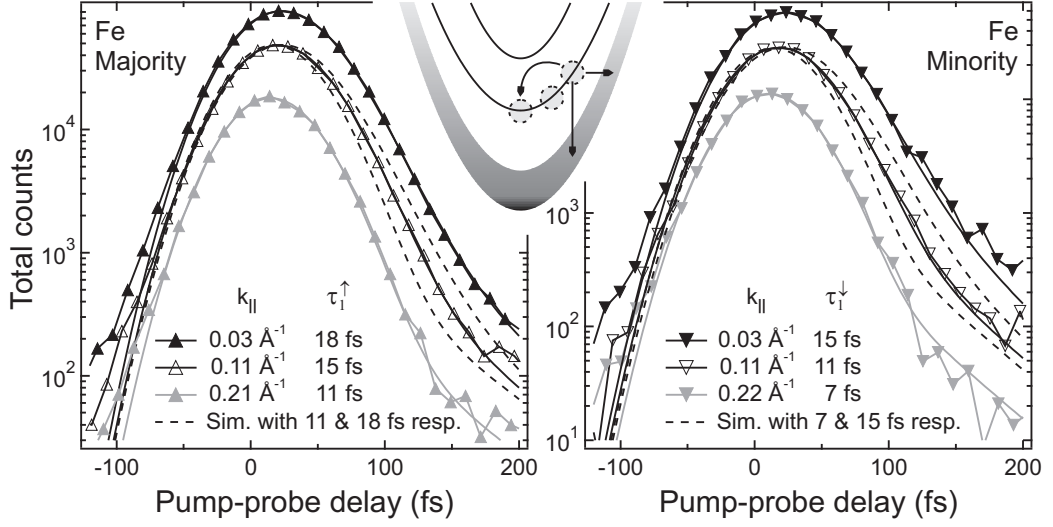[8]More precisely, scattering due to imperfections of the iron or cobalt surface such as steps, adatoms and vacancies.

Figure 4.23: Time-resolved 2PPE spectra of the $n = 1$ image-potential state on iron at three different points in k-space measured with an excitation energy of $\hbar\omega_a = 4.85$ eV. With increasing parallel momentum $k_\parallel$, the lifetime of the image-potential states decrease. Simulations with optical Bloch equations (solid lines) yield the indicated lifetimes. For comparison, the simulated traces adapted the two other spectra (dashed lines) have been plotted alongside the proper simulation for the data measured at $k_\parallel = 0.11$ Å^{-1}.

scattering is barred to majority-spin electrons. This explains nicely why we do not observe quasi-resonant interband scattering via magnon-absorption into the minority-spin $n = 1$ image-potential state, but a strong component from interband scattering in the majority-spin channel.

We now have established that on iron dephasing and resonant interband scattering are spin dependent. The underlying microscopic process is in all probability quasielastic electron-magnon scattering. In the next section we will show that also inelastic scattering is significantly influenced by magnon emission.

4.6.2 Spin-dependent intraband scattering

With increasing momentum parallel to the surface, i.e. increasing energy above the band minimum, the lifetime of the image-potential-state electrons decreases significantly in both spin channels. Figure 4.23 features three representative traces of time-resolved 2PPE measurements at three different points on the image-potential band. Obviously the cross-correlation trace is narrowest, i.e. the lifetime is shortest, for the highest parallel momentum $k_\parallel$

in both spin channels. All time-resolved data have been simulated with optical Bloch equations, yielding the respective lifetimes shown in Figure 4.23. The difference between the spectra becomes evident if we concentrate on the data for $k_{\parallel} = 0.11$ Å^{-1}. Here the traces simulated for the other two spectra at lower and higher energy are shown in addition to the corresponding simulation. The significance of a lifetime difference of three to four femtoseconds becomes immediately obvious.

Thinking back to the lifetimes presented in Section 4.2, the reader may wonder why the lifetime of the $n = 1$ image-potential state at $k_{\parallel} = 0.03$ Å^{-1} shown in Figure 4.23, i.e. almost at the minimum of the band, is *larger* than the lifetimes $\tau_1^{\uparrow} = 16$ fs and $\tau_1^{\downarrow} = 11$ fs claimed in Section 4.2 for $k_{\parallel} = 0$, although it should *decrease* with increasing $k_{\parallel}$. It has already been mentioned that the observation of intermediate states closer to E_{vac}, like the $n = 1$ image-potential state at larger parallel momentum for example, requires a sufficiently high excitation energy. Consequently, the image-potential band is filled not only at the band minimum, as was the case for the time-resolved measurements shown in Figure 4.4, but up to an energy of $E_F + \hbar\omega_a$.

Electrons high up in the image-potential band have an alternative to decay into the bulk, they may also relax towards the band minimum, remaining within the image-potential band. Due to the large spatial overlap of the image-potential wave-functions[9] in comparison with the overlap of an image-potential with a bulk wave-function, this intraband scattering process contributes strongly to the increasing decay rate with increasing $k_{\parallel}$ [16]. The band minimum is therefore permanently being refilled from states with a shorter lifetime.

Refilling from states with a longer lifetime, e.g. interband scattering from the $n = 2$ image-potential state, becomes manifest in a biexponential decay with the longer lifetime dominating at large pump-probe delay. In contrast, refilling from states with a shorter lifetime is visible only at small pump-probe delay and usually difficult to detect at all unless it is pronounced. A first glance at the spectra in Figure 4.24 might lead the unsuspecting experimentalist to simply believe in a longer lifetime of the $n = 1$ image-potential state at the band minimum, if measured with a higher photon energy $\hbar\omega_a$. Of course this would be strange indeed. A Bloch-equation trace simulated with the respective lifetimes determined in Section 4.2, as well as a simulation with additional interband scattering from the $n = 2$ image-potential state,

---

[9]The z component of the image-potential-state wave function depends only on the position of the image-potential state in the surface-projected band gap, which changes only slightly with $k_{\parallel}$.
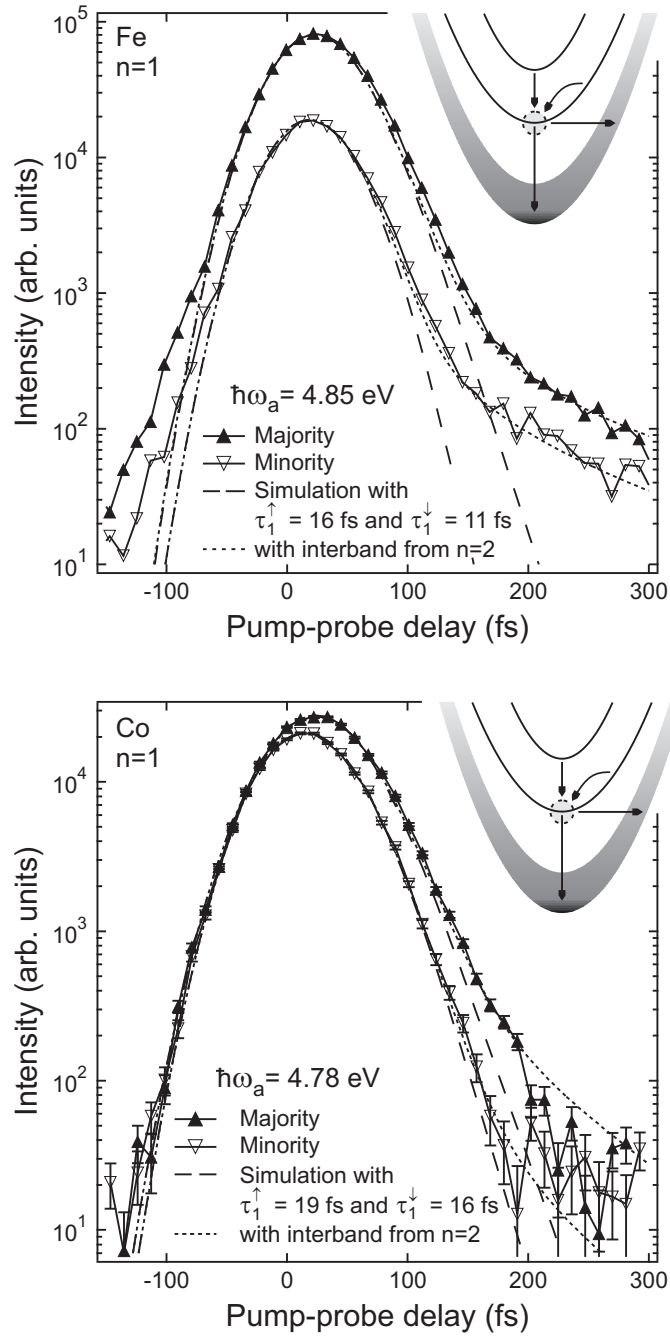
Figure 4.24: Time-resolved 2PPE measurement of the $n = 1$ image-potential state on iron (top graph) and cobalt (bottom graph) with a high excitation energy $\hbar\omega_a$. The two simulations (dashed lines without, dotted lines with interband scattering from the $n = 2$ image-potential state) were done using optical Bloch equations and the lifetimes determined in Section 4.2. Refilling from states with $k_\parallel > 0$ are the cause of the increased intensity at small pump-probe delay.

are shown for comparison. The slightly higher intensity at small pump-probe delay, easier to spot in the iron spectra, can not be described with a simple exponential decay, but indicates refilling from a short-lived state. Refilling of a state with electrons from states with a smaller lifetime simulates (*not* in the sense of numerical simulations) a seemingly longer lifetime. It should therefore be noted that especially the decay rates at the band minimum measured with a high excitation energy in this section are slightly underestimated. On Cu(100) for example, the lifetime of the $n = 1$ image-potential state was found to be $\tau = 40$ fs if measured with a high excitation energy while a low excitation energy yielded $\tau = 36$ fs [16]. This effect poses in fact a major problem for the experimental determination of bulk-electron lifetimes near E_F with 2PPE. In the bulk, refilling processes usually can not be avoided, rendering a reliable determination of decay rates at least a challenge.

To return to the momentum-dependent lifetimes of image-potential states on the ferromagnetic surfaces, let us have a look at Figure 4.25. The decay rate $\Gamma_1 = 1/\tau_1$ plotted versus the energy above the band minimum of the $n = 1$ image-potential band reveals a linear increase of the decay rate with energy on both material systems and for majority- as well as minority-spin electrons. So far this has already been observed on the Cu(100) surface: Literature provides reference values for the slope of the $n = 1$ image-potential-state decay rate of $d\Gamma/dE = 0.07$ (eVfs)$^{-1}$ [16] and $d\Gamma/dE = 0.05$ (eVfs)$^{-1}$ [22]. The values we obtained on Co lie in the same range with a slope of $d\Gamma^{\downarrow}/dE = 0.08$ (eVfs)$^{-1}$ for minority-spin electrons and $d\Gamma^{\uparrow}/dE = 0.06$ (eVfs)$^{-1}$ for the majority-spin electrons.

On iron the increase in the decay rate is not only much stronger, but the difference between the majority- and minority-spin image-potential band is much more pronounced, the minority-spin slope $d\Gamma^{\downarrow}/dE = 0.25$ (eVfs)$^{-1}$ is twice as large as the slope $d\Gamma^{\uparrow}/dE = 0.12$ (eVfs)$^{-1}$ for majority-spin electrons.

For the decreasing lifetime of the image-potential state on Cu(100) with parallel momentum, two major decay channels were named responsible [16]. Electrons may either decay into the bulk states via electron-electron scattering, thereby exciting an electron in the bulk, or via intraband decay. On Cu(100), both processes contribute almost equally strong to the increase in decay rate with energy. Both processes are the result of a larger phase space available for scattering, though on very different energy scales.

This can be understood with a look at Figure 4.26. The image-potential states lie roughly 4 eV above the Fermi energy. Consequently an electron decaying from an image-potential band into the bulk via electron-electron
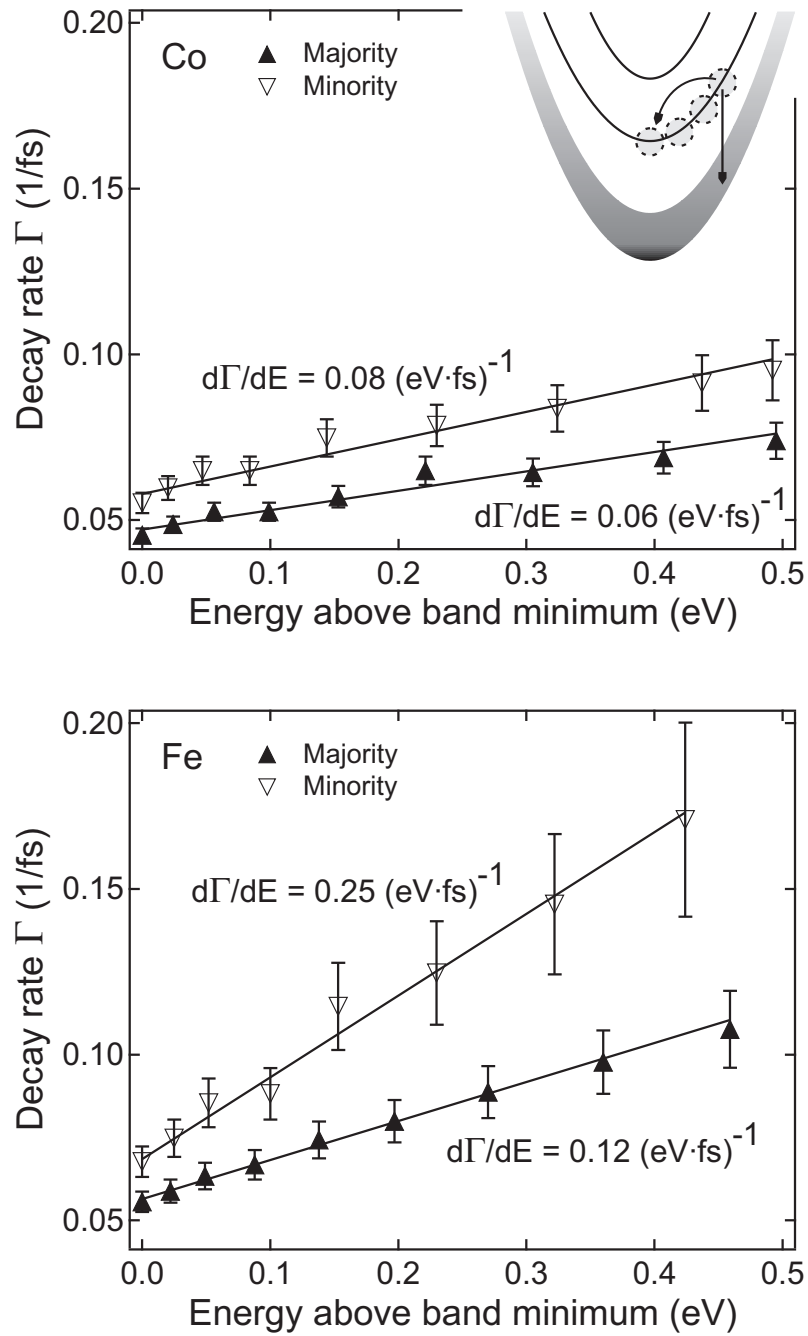
Figure 4.25: Decay rate Γ_1 of the $n = 1$ image-potential states on cobalt (top) and iron (bottom) in the majority (▲) and minority (▽) band for increasing energy above the band minimum. The measurements were carried out with the same excitation energies as noted in Figure 4.24. The inset schematically depicts intraband decay (bent arrow) and decay into the bulk bands (vertical arrow), as well as representative points on the dispersing bands (dashed circles), where the decay rate was determined.
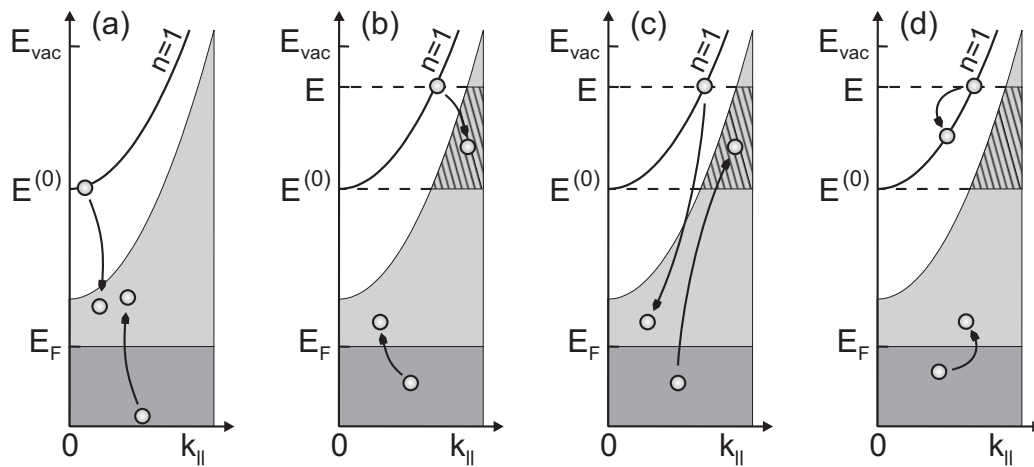
Figure 4.26: Schematic of the free-electron like dispersion parallel to the surface of the $n = 1$ image-potential state in the gap of the surface-projected bulk bands (gray area). Decay from the minimum of the image-potential band into the bulk via electron-electron scattering, i.e. excitation of another electron is indicated on the left (a). The hatched area illustrates the additional phase space available for an electron at E above the band minimum $E^{(0)}$; cf. panels (b) and (c). The energy transfer during intraband decay, which is depicted in panel (d), is usually much smaller than for decay into the bulk.

scattering to states close to E_F, where unfilled d bands provide a large number of empty states, must lose these 4 eV in the process, supplying its scattering partner with said 4 eV of energy. Such an event is sketched in Figure 4.26(a). For an electron at the band minimum $E^{(0)}$ all states within $E^{(0)} - E_F$ are in principle available for scattering into. Hence, an electron at $E > E^{(0)}$ gains additional phase space for decay (schematically indicated with the hatched areas in Figure 4.26(b) and 4.26(c)), which is one part of the reason why the decay rate of image-potential-state electrons increases. Incidentally, the processes indicated in Figure 4.26(b) and 4.26(c) interfere, as there is no way to distinguish whether the image-potential state electron has decayed in a *direct* process into the *sp* states (b) or has been *exchanged* with a bulk electron (c).

During intraband decay, on the other hand, an electron at energy E can at most lose the amount of energy it resides above the band minimum, i.e. $E - E^{(0)}$ and of course only transfer this much to the bulk electron excited in the process (cf. the sketch in Figure 4.26(d)). With a look at the energy scale of Figure 4.25, we find this an order of magnitude below the energy that may be transferred during scattering into the bulk.

With these processes in mind, we will now establish why it may seem surprising that first, the decay rate increases so much more on iron than on cobalt, and second that the minority-spin slope is larger than the majority-spin slope.

To estimate the lifetime $\tau^\sigma(E)$ of an electron with spin $\sigma \in \{\uparrow, \downarrow\}$ at energy E above E_F, a semiempirical method based on perturbation theory and the density of states $\rho^\sigma(E)$ is often employed, e.g. in [126, 128, 124, 45, 189, 93, 194]. The decay rate $\Gamma^\sigma = 1/\tau^\sigma$ of an excited "primary" electron can be calculated using Fermi's golden rule, as

$$\Gamma^\sigma(E) = \frac{2\pi}{\hbar} \int_{E_F}^{E} dE' \rho_>^\sigma(E') \int_0^{E_F} d\varepsilon [\rho_<^\sigma(\varepsilon)\rho_>^\sigma(\varepsilon + \omega)|M_C^{\sigma\sigma}|^2$$
$$+ \rho_<^{\bar\sigma}(\varepsilon)\rho_>^{\bar\sigma}(\varepsilon + \omega)|M_C^{\sigma\bar\sigma}|^2] , \qquad (4.17)$$

where $\omega = E - E'$ is the energy transfer and $\bar\sigma$ the spin opposite to σ. $\rho_<^\sigma(\varepsilon) = \rho^\sigma(\varepsilon)f(\varepsilon)$ and $\rho_>^\sigma(\varepsilon) = \rho^\sigma(\varepsilon)[1 - f(\varepsilon)]$ denote the number of occupied and unoccupied electronic states, respectively, with the Fermi-Dirac distribution $f(\varepsilon)$ accounting for the occupation probability of a state at energy ε. This is illustrated in Figure 4.27.

This model is sometimes referred to as DOS convolution model, because it includes a convolution of the density of states, i.e integrates over the empty states available for the primary electron to scatter into and simultaneously
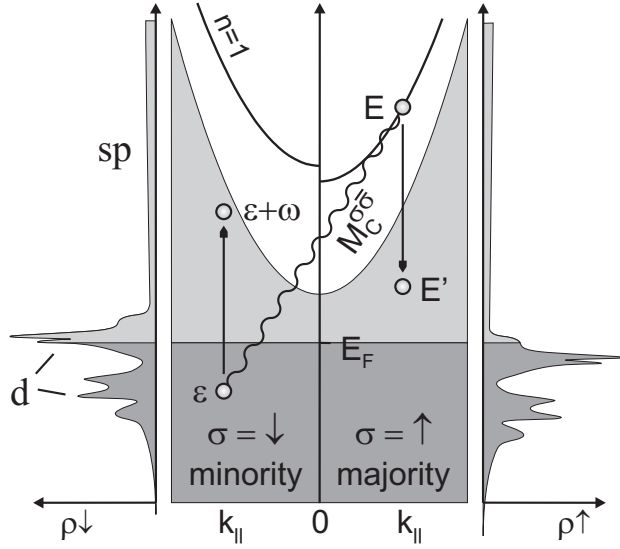
Figure 4.27: Diagram of a decay process accompanied by an electron-hole pair creation in the opposite spin channel as described in Equation 4.17 by the transition matrix element $M_C^{\sigma\bar{\sigma}}$. Also shown is the schematic density of states $\rho^{\uparrow\downarrow}$ for a weak ferromagnet.

accounts for the accessible phase space of the secondary electrons excited through the interaction.

The latter play a vital role in the relaxation dynamics of hot electrons. Hot electron lifetimes in Cu for example refuse to obey the $(E-E_F)^{-2}$ dependence predicted by the Fermi-liquid theory for free-electron metals. They deviate strongest once the electrons from the d bands 2 eV below E_F participate in the scattering [120]. It thus becomes clear that it is often not sufficient to consider the d holes only to describe the decay of excited electrons.

The matrix elements $|M_C^{\sigma\sigma}|^2$ ($|M_C^{\sigma\bar{\sigma}}|^2$) describe the screened Coulomb interaction between two electron-hole pairs in the same (in opposite) spin channel(s), i.e the decay of an electron with spin σ into an empty state, thereby exciting an electron with spin σ ($\bar{\sigma}$) into an unoccupied state. The Coulomb matrix elements M_C should not to be confused with the dipole matrix elements M_{fi} introduced in Equation 3.4.

For the matrix elements as employed in Equation 4.17, the interference between direct and exchange terms[10] has been neglected [126] and the "random-

---

[10]Due to the indistinguishability of electrons *with the same spin*, there is no way of knowing whether an electron has decayed, e.g., via process (b) or via process (c) as shown in Figure 4.26. While process (b) is called direct, process (c) is called exchange scattering. Note that for process (d) also a corresponding exchange process exists. In other words,

k" approximation[11] employed [12, 86]. Usually the energy dependence is also neglected, i.e. $M_C \neq M_C(\omega)$.

For the interpretation of experimental data with the help of the DOS convolution model, these matrix elements are more or less employed as parameters to fit measured data. Spin-dependent electron dynamics have been described by assuming various values for the probability of spin-singlet scattering (scattering of two electrons with antiparallel spin $|M_C^{\sigma\bar{\sigma}}|^2$) versus spin-triplet scattering (scattering of two electrons with parallel spin $|M_C^{\sigma\sigma}|^2$) [45, 93], and/or the distinction between sp and d electrons [189, 93]. The latter accounts especially for the different overlap between the wave functions of sp and d electrons, which naturally results in different matrix elements for scattering between sp electrons, between d electrons, or between sp and d electrons.

While we will not attempt to calculate any spin-dependent lifetimes here, mainly because not even the band structure of our thin films is known, we can employ the argumentation of the DOS convolution model to study the trends in our data qualitatively. Especially the spin-dependent increase of the image-potential-state decay rate will demand our attention.

For the benefit of the reader familiar with image-potential-state dynamics, it should be noted here that a scaling of the slope $d\Gamma/dE$ with the decay rate at the band bottom $\Gamma(k_\parallel = 0)$, as found for image-potential states on noble gas covered Cu surfaces [184, 16, 145], is not applicable in our case here. The scaling is a consequence of the decreasing overlap of the image-potential-state wave function with the bulk for increasing layer thickness, which reduces the interaction strength for all decay channels alike, but has no influence on the available phase space.

In our case the spin-dependent inelastic decay of the image-potential-state electrons via screened Coulomb interaction involves sp and d bulk states. The latter mainly determine the difference in majority and minority decay rate. Given the small exchange splitting of the image-potential state, the contribution of the (spin-dependent) bulk penetration of the image-potential-state wave function to the spin dependence of the decay rate is negligible.

---

an image-potential state electron may decay either remaining within the image-potential state and exciting another electron in the bulk, or scattering into the bulk exciting a bulk electron into the image-potential state. These processes interfere as initial and final state of the scattering process are indistinguishable. Of course there is no interference term between direct and exchange scattering in $|M_C^{\sigma\bar{\sigma}}|^2$, as direct scattering from one spin channel into the other is not possible via Coulomb scattering.

[11]In this approximation the matrix element describing the screened interaction is replaced by a value, which only depends on the exchanged energy, but is averaged over **k** and the exchanged momentum, thus effectively ignoring momentum conservation.

Therefore the scaling $d\Gamma/dE \propto \Gamma(k_\parallel = 0)$ does not hold for the majority- and minority-spin component and the observed spin-dependent slopes can not be attributed to the spin-dependent decay rate at the band minimum.

All empty states from the Fermi energy to the image-potential-state energy $E^{(0)}$, and all filled states within the same energy interval below E_F, contribute to the decay rate $\Gamma(k_\parallel = 0)$ measured at the minimum of the image-potential band, approximately 4 eV above E_F. The dynamics of transition metal electrons are dominated by the d states with their high density of states, and for our thin iron and cobalt films, the $3d$ bands lie within the ± 4 eV interval around E_F. Thus the phase space an electron above the band minimum gains, pertains mainly to sp states. Here we discuss the *increase* of the decay rate, i.e. the decay rate *added* to $\Gamma(k_\parallel = 0)$. The convoluted DOS up to the band minimum is already accounted for in the spin-dependent decay rate at $E^{(0)}$. An electron residing at an energy $E > E^{(0)}$ above the band minimum, which decays to the Fermi energy, i.e. with a large energy transfer ω, may now excite occupied bulk d electrons $\Delta E = (E - E^{(0)})$ higher into the sp band than an electron decaying from the band minimum (cf. Fig. 4.26(c)). Also electrons from ΔE further below E_F, where only sp bands are found, may now be excited into empty d states above E_F. Because the density of states of the sp bands is almost spin *in*dependent, the *increase* in decay rate for these processes should also be more or less spin *in*dependent.

For the same reason, direct scattering from the image-potential state into the additional empty sp states between E and $E^{(0)}$ (hatched area in Fig. 4.26) should also not generate a spin-dependent increase of the decay rate.

Though in this case the phase space for the primary electron may not be spin dependent, possible excitations for the secondary electron occur around the Fermi level, where low energy excitations from the minority-spin d states below into the empty minority d states above E_F dominate. If we assume that a primary electron excites a secondary electron of the same spin equally likely as of the opposite spin, i.e. $|M_C^{\sigma\bar\sigma}|^2 = |M_C^{\sigma\sigma}|^2$, any differences between the probability for secondary electron excitation in the majority- or minority-spin channel are of no consequence. However, exchange usually weakens the interaction between parallel-spin electrons, and it is often assumed that spin-singlet scattering is far more likely than spin-triplet scattering, i.e. $|M_C^{\sigma\bar\sigma}|^2 \gg |M_C^{\sigma\sigma}|^2$ [31, 126, 88, 93, 192]. Then the excitation of secondary minority-spin electrons would be much more probable for a majority-spin image-potential-state electron decaying into the bulk with only a small energy transfer, than for a minority-spin image-potential-state electron.

The same is true for intraband decay. The image-potential state is localised

perpendicular to the surface, dispersing free-electron like parallel to the surface. The density of states of such a two-dimensional electron gas is constant. With the same effective mass for majority- and minority-spin electrons in the image-potential state, both have the same phase space available for intraband decay. Due to the Pauli principle, spin-majority electrons scatter preferentially with spin-minority electrons, and there is much phase space available for secondary electron-hole pair creation in the minority-spin channel.

With these arguments in mind, we would expect a similar slope $d\Gamma/dE$ in both spin channels, if not a larger increase of the majority-spin decay rate than the minority-spin decay rate. We do not predict a higher decay rate for majority electrons but merely a similar, if not stronger increase of the decay rate. As can be seen from Figure 4.25, this is clearly not the case.

Instead, we observe a slightly stronger increase in the minority-spin channel on cobalt and, most noticeably, the minority-spin slope is twice the majority-spin slope on iron. Obviously the (mean) slope on Co is fairly comparable to the one measured on Cu, which supports our argument, that mainly additional phase space in the *sp* bands is gained above the minimum of the image-potential band $E^{(0)}$, and thus the difference between Co and Cu is small.

Up to now we have confined our decaying electrons firmly within one spin channel. If we consider the emission of magnons, on the other hand, minority-spin electrons decaying within the image-potential band could acquire twice the phase space a majority-spin electron gains. A minority-spin electron could decay via intraband scattering within the (minority-spin) image-potential band *and* via magnon emission into the majority-spin image-potential state. The latter is for the most part sufficiently inelastic that magnon absorption for majority-spin electrons is unlikely at the liquid nitrogen temperature of our sample. Therefore, a *majority*-spin image-potential-state electron can only decay along the *majority* band. The doubling of the phase space for the decay of *minority*-spin as compared to majority-spin image-potential-state electrons upon magnon emission most conveniently explains the doubling of the slope of the decay rate in iron.

Already for spin-dependent dephasing and spin-dependent resonant interband scattering, electron-magnon scattering commended itself as a likely cause, in both instances virtually nonexistent in the cobalt film and strong in iron. Finding similar behaviour for intraband scattering is therefore quite suggestive of magnon emission as the same source.

There is, however a slight drawback to this explanation, which we have concealed so far. The emission of a magnon would require a spin flip of
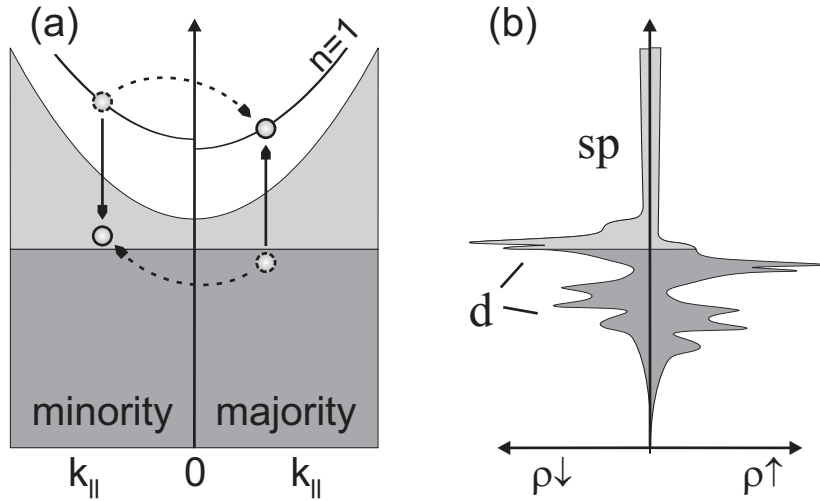
Figure 4.28: (a) Schematic illustration of an exchange process leading to an electron of opposite spin in the image-potential band. A direct process with spin flip, as indicated by the dashed arrows, is not allowed in screened Coulomb interaction, because in such a case angular momentum would have to be exchanged. (b) The schematic density of bulk states $\rho^{\uparrow\downarrow}$ shows that such a process may be strong due to the high density of empty minority- and filled majority-spin states.

the image-potential-state electron to scatter from the minority-spin into the majority-spin band. Unfortunately Coulomb interaction does not mediate such a spin flip, it is spin conserving. We will establish in the next section, why we nevertheless observe magnon emission in iron.

4.6.3 Magnon-enhanced exchange scattering

The only way for an electron to appear in the majority-spin image-potential band, when it previously resided in the minority-spin band, is via an exchange process. The primary minority-spin electron would decay into the bulk, exciting a secondary majority-spin electron into the image-potential state instead. Such an exchange process of electrons with antiparallel spin leaves a minority-spin electron above E_F and a majority-spin hole below E_F behind, a configuration commonly known as Stoner pair. The exchange process leading to the excitation of a Stoner pair is illustrated in Figure 4.28. At first, it may seem very unlikely for a secondary bulk electron to be excited into the image-potential band of all states. But in the decay process four electronic states participate, the primary electron and hole, as well as the

secondary electron and hole. In terms of probability for the secondary electron to be excited into an image-potential-state hole, the large spatial overlap between image-potential-state wave functions may very well balance the high density of states (but small spatial overlap with the image-potential-state) in the bulk. Remember that on Cu(100) decay within the image-potential band contributes about 50% to the overall intraband decay rate.

For the interpretation of spin-polarised electron-energy-loss (SPEELS) experiments, for example, exchange[12] has to be taken into account. It turned out that for electrons scattered inelastically off a metal, the importance of such an exchange process may be comparable to direct (non-flip) processes at low primary beam energies [88, 175, 127, 112, 1].

Additionally it was pointed out as early as 1985 [175] that the spin-flip cross section in SPEELS spectra may even be dominated by collective modes (magnons), providing a possibility to measure magnon dispersion by this technique. It took until 2003 for the first spin-wave dispersion curves to be determined experimentally with SPEELS [176], because only for very low primary beam energies (≤ 10 eV), magnons appear in the loss spectra.

To understand how magnon emission occurs, though direct spin-flip scattering from such a collective mode is not possible, we have to engage a little in modern *ab initio* methods for the calculation of lifetimes of excited electrons based on the self-energy formalism of many-body theory (Of course this detour will remain firmly on a pedestrian, or rather experimentalist level.). The self-energy can be understood as the potential, which is felt by an electron ("test charge" or primary electron) added to a many-body system (e.g. a metal). This potential arises from the response of the other electrons to the presence of the additional electron. In a sense, the electron is interacting with itself via the many-body system, thus changing its own energy. Note that exchange processes, which occur in a system of indistinguishable particles, are also included in the self-energy. In the framework of many-body theory, the decay rate $\Gamma = \tau^{-1}$ of an excited electron can be derived from

---

[12]In the context of SPEELS (and now also 2PPE) measurements, the term "exchange" is usually employed not in the correct sense of indistinguishable Fermions in a many-body system, but from the point of view of the experiment. Then exchange is used to describe the decay of an electron into the bulk and the simultaneous excitation of a bulk electron into the image-potential state or the free electron state. If the excited (secondary) bulk electron has spin opposite to the primary electron, this is detected in the experiment as an apparent spin flip. As such an "exchange" can be measured, it can not be an exchange process in the original sense, but an image-potential-state electron or an electron from the impinging beam has been exchanged for a bulk electron.
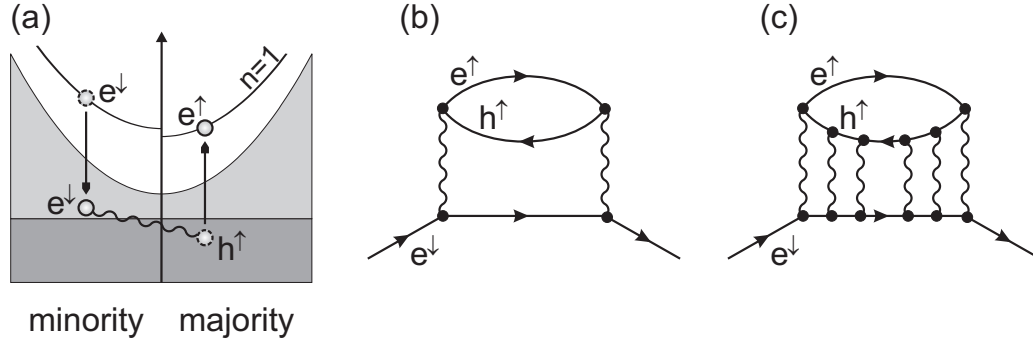
(a)

minority   majority

(b)

(c)

Figure 4.29: (a) Schematic illustration of the interaction (wiggly line) be-tween the scattered image-potential-state electron and the hole created in the decay process. (b) Feynman diagram for the contribution of electron-hole-pair creation in the spin-majority channel to the self-energy of a minority-spin electron. (c) Feynman diagram of the final-state interaction depicted in (a); magnon emission as a collective excitation corresponds to (multiple) scatter-ing between the primary electron and the hole of an electron-hole pair in the opposite spin channel (Feynman diagrams after Refs. [78] and [193, 195, 192]).

the imaginary part of the electron self-energy Σ as

$$\Gamma = -\frac{1}{\hbar}\text{Im}\Sigma \; , \tag{4.18}$$

while the real part determines the dispersion relation of the electron in the presence of the rest of the metal, i.e. the band structure [107, 188, 51].

In the widely used GW approximation, the self-energy is expanded in a per-turbation series of the (spin-independent) screened Coulomb interaction W, and only the first term in the series expansion is retained [51, 196]. This approximation is well suited for systems where long-range screening is preva-lent, but short-range interactions are not properly described. Among the latter are the short-range hole-hole interactions, which describe the satel-lite structure in the photoemission spectra of, e.g., the strongly correlated ferromagnet nickel [69]. Interaction of the primary electron with an electron-hole pair excited in the opposite spin channel, as shown in Figure 4.29(a), is also not included in the GW approximation [196]. Such shortcomings led to an extension of the GW approach with the T-matrix formalism to include multiple electron-electron, hole-hole and electron-hole scattering [165, 195]. When dealing with ferromagnets, $GW + T$ proves especially powerful, be-cause this theory also accounts for the contributions of spin-wave emission to the self-energy of an excited electron.

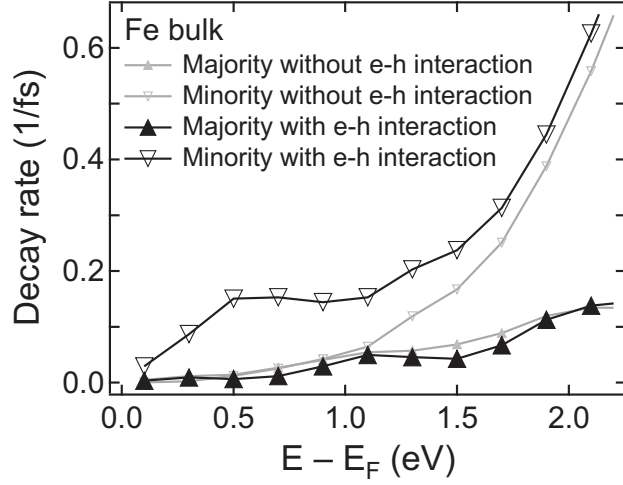Though the T-matrix adds only higher-order terms to the self-energy [107],

Figure 4.30: Spin-dependent decay rate of excited electrons in bcc bulk iron as a function of energy above E_F calculated with the $GW + T$-matrix formalism. For the grey traces with small symbols, amongst others Stoner-pair creation was allowed, while for the black curves (large symbols) also magnon emission, i.e. multiple electron-hole interaction was included. These data (from Ref. [193]) were kindly provided by V. Zhukov.

the impact of multiple electron-hole scattering on lifetimes calculated for iron are huge. Figure 4.30 displays the inverse lifetimes of hot electrons in bcc bulk iron derived from first-principles calculations that fully include the band structure of the solid. The calculated data shown in Figure 4.30 were originally published in Reference [193] and kindly provided by V. Zhukov [192]. The grey traces represent decay rates of majority- and minority-spin electrons as a function of excitation energy above E_F with $GW + T$ matrix contributions, but without interaction of the primary electron with the hole of an excited electron-hole pair, i.e. without the inclusion of spin-wave emission. For the calculation of the decay rates depicted as black symbols, magnon emission was included. For the minority-spin hot-electron lifetime at excitation energies below 1.5 eV, the contributions of multiple electron-hole interactions can clearly not be neglected.

Other contributions of the T matrix are comparatively small. Here we follow the argumentation brought forward by V. Zhukov and coworkers [193, 192]. Due to exchange, the T matrix contributions within one spin channel are small, because direct and exchange terms cancel at least partially, or, to put it simply, the Pauli principle reduces the interaction of electrons with the same spin. In a ferromagnet, the interaction of a minority-spin primary electron with the *electron* of an excited electron-hole pair in the opposite

spin channel is much smaller than the interaction with the *hole* of the excited electron-hole pair. While the latter will be dominated by the convolution of empty minority-spin *d* states with filled majority-spin *d* states, for the former the convolution will be with empty majority-spin *sp* states (cf. Fig. 4.28).

The relative importance of Stoner-pair creation and spin-wave scattering for inelastic electron scattering in metals was already pointed out in earlier publications [136, 137, 78, 147]. The approach of incorporating final-state interactions between the excited electron and hole in the bulk to introduce collective excitations (magnons) yielded a dominating contribution of magnon emission at low excitation energies.

We have now established the relevance of spin-wave emission for low primary electron energies in SPEELS experiments and low excitation energies in the bulk ferromagnet. We argue that the situation in an electron-energy-loss experiment is comparable to image-potential-state electrons inelastically scattering with bulk states. With the observation of spin-dependent intraband scattering, we have experimental access to low-energy excitations in the bulk. Note that our measurements are not obscured by an elastic peak at very low energy transfer, as in SPEELS experiments, and we operate directly in the time domain.

In our case, the most important contributions are presumably the terms accounting for an electron-hole-pair creation in the opposite spin channel and the interaction of the primary electron with the hole of the excited electron-hole pair. Figure 4.29 features the corresponding Feynman diagrams of Stoner excitation (b) and collective modes (c). With a glance at the schematic density of bulk states depicted in Figure 4.28(b) it can be understood that the former process may be strong due to the high density of empty minority- and filled majority-spin states. Theoreticians also propose a huge contribution to the self-energy of a minority-spin electron from (multiple) interaction with the hole of the created electron-hole pair (cf. Fig. 4.29(c)). From the point of view of an image-potential-state electron, magnon emission therefore enhances the probability of exchange scattering with spin flip, i.e. magnon emission occurs via a final-state interaction.

The energy losses in intraband scattering of $0-500$ meV lie within the energy range where spin-wave emission dominates. So magnon emission may very well accompany intraband decay of minority-spin electrons with an apparent spin flip and explain the factor of two in the increase of the decay rate of the minority-spin electrons compared with the majority-spin electrons in the image-potential band.

Spin-wave emission might also explain why we observe a larger ratio of

majority- to minority-spin-electron lifetimes in iron than in cobalt [151] though the bandstructure measurements performed by my colleague M. Pickel indicate that the Co thin film, like its bulk counterpart, is a strong ferromagnet with a high density of minority-spin d holes and no majority-spin d holes. The calculations of V. Zhukov and coworkers show that the bandstructure alone is not sufficient to fully account for spin-dependent lifetimes in iron, but the excitation of collective modes represents an additional channel, which increases the asymmetry between majority- and minority-spin lifetimes [193]. In nickel, the effects of an apparent spin flip are much smaller. Unfortunately the author is not aware of a comparable study for cobalt.

Our measurements, however, never yielded any hints of spin-wave scattering on cobalt. Neither dephasing, resonant interband scattering nor intraband scattering prove to be as highly spin dependent as on iron. It seems that on iron electron-magnon interaction is already relevant at the minimum of the image-potential band and there are obviously no indications of an energy threshold for magnon emission on the iron thin film.